

# Resource Allocation in Hybrid Radio-Optical IoT Networks using GNN with Multi-task Learning

Aymen Hamrouni<sup>1</sup>, Student Member, IEEE, Sofie Pollin<sup>1</sup>, Senior Member, IEEE, and Hazem Sallouha<sup>1</sup>, Senior Member, IEEE

<sup>1</sup>WaveCore at the Department of Electrical Engineering (ESAT), KU Leuven, Belgium.  
E-mails: {aymen.hamrouni, sofie.pollin, hazem.sallouha}@kuleuven.be.

Corresponding author: Aymen Hamrouni (email: aymen.hamrouni@kuleuven.be).

This work was supported in part by the SUPERIOR project (SNS JU under the European Union's Horizon Europe research and innovation program, Grant Agreement N°101096021) and the 6thSense project (HORIZON-MSCA-DN-2022, Grant Agreement N°101119652).

**ABSTRACT** This paper addresses the problem of dual-technology scheduling in hybrid Internet-of-things (IoT) networks that integrate Optical Wireless Communication (OWC) alongside Radio Frequency (RF). We begin by presenting an optimization formulation that jointly considers throughput maximization and delivery-based Age of Information (AoI) minimization between access points and IoT nodes under energy and link availability constraints. However, given the intractability of solving such NP-hard problems at scale and the impractical assumption of full channel observability, we propose the Dual-Graph Embedding with Transformer (DGET) framework, a supervised multi-task learning architecture combining a two-stage Graph Neural Networks (GNNs) with a Transformer-based encoder. The first stage employs a transductive GNN that encodes the known graph topology and initial node and link states (e.g., energy levels, available links, and queued transmissions). The second stage introduces an inductive GNN for temporal refinement, which learns to generalize these embeddings to the evolved states of the same network, capturing changes in energy and queue dynamics over time, by aligning them with ground-truth scheduling decisions through a consistency loss. These enriched embeddings are then processed by a classifier for the communication links with a Transformer encoder that captures cross-link dependencies through multi-head self-attention via classification loss. Simulation results show that hybrid RF-OWC networks outperform standalone RF systems by handling higher traffic loads more efficiently and reducing AoI by up to 20%, all while maintaining comparable energy consumption. The proposed DGET framework, compared to traditional optimization-based methods, achieves near-optimal scheduling with over 90% classification accuracy, reduces computational complexity, and demonstrates higher robustness under partial channel observability.

**INDEX TERMS** IoT, Wireless Optical, Radio Frequency, AoI, Optimization, Graph Neural Networks, Transformers

## I. Introduction

### A. Motivation

IN recent years, the proliferation of Internet-of-things (IoT) devices has revolutionized the way we live and work. From wearable gadgets that monitor our health to smart home systems that enhance our living environment, the ubiquity of IoT technologies is undeniable. One key challenge in IoT networks lies in the efficient collection and transmission of data in real-time [1], [2]. For instance, in healthcare, IoT enables continuous remote monitoring

of critical patient vitals, such as heart rate and blood pressure, requiring prompt transmission for timely medical interventions [3], [4]. Industrial IoT (IIoT) requires real-time data transmission for monitoring machinery and production lines, enabling preemptive maintenance [5]. Another key challenge in IoT networks is energy efficiency. Many devices are low-powered or even batteryless [6], relying on energy harvesting. While prompt data transmission is crucial, the energy consumption involved in this process must also be taken into account as it significantly impacts the long-term

operation of IoT devices. Conventional IoT networks mainly rely on single-band Radio Frequency (RF) technologies, such as Bluetooth Low Energy (BLE) at 2.4 GHz, which are designed for low-power operation [7] but operate in a heavily shared spectrum, suffering from congestion, interference, and limited bandwidth [8]. These effects become particularly severe in dense deployments [9].

Multi-band communication is a promising solution [10]–[12] for next-generation IoT networks. By leveraging the use of multiple communication bands, such as a combination of RF bands and Optical Wireless Communication (OWC) technologies (e.g., visible light, infrared), multi-band networks can allow IoT devices to dynamically select the most suitable band based on real-time factors such as the IoT application’s data rate and latency requirements, environment, or the devices’ condition (e.g., energy budget). The intelligent integration of RF and OWC in a hybrid system has the potential to exploit their complementary strengths. RF remains essential for providing long-range connectivity and non-line-of-sight (NLoS) communication, whereas OWC, operating in visible light, infrared, or terahertz (THz) bands, offers high-capacity, low-latency, and interference-free communication [13]. Such integration not only mitigates congestion in heavily utilized bands but also improves resilience by providing an alternative communication medium in case of network failures [14]. Optical components such as infrared LEDs and photodetectors are low-cost, energy-efficient, and widely available, making hybrid RF-OWC architectures feasible with limited additional hardware complexity [15], [16]. Fig. 1 illustrates a smart hospital scenario with multiple access points (APs) and IoT nodes equipped with RF and OWC, where RF supports general wireless connectivity and OWC is used in sensitive areas such as MRI rooms to avoid RF interference. Recent works [13], [16] have demonstrated the practical feasibility of RF-OWC IoT networks that combine RF and Visible Light Communications (VLC) for data transfer and energy harvesting, enabling battery-less or ultra-low-power operation.

Despite the enormous advantages, the integration of RF and OWC technologies into a unified hybrid communication system presents several challenges in optimizing the RF-OWC resources allocated to serve IoT nodes. First, OWC and RF have different propagation characteristics, processing, and energy profiles, increasing the optimization problem complexity. This challenge becomes even more pronounced when considering practical IoT implementations that often involve dual and sometimes conflicting objectives, such as maximizing network throughput while minimizing latency. Second, the scalability of the hybrid RF-OWC resource allocation solution is particularly critical in IoT networks due to networks typically consisting of multiple APs, with the number of IoT nodes being at least an order of magnitude higher [17]. Moreover, seamless integration of RF and OWC technologies requires adaptive and context-aware resource management that can respond to varying link quality, dy-

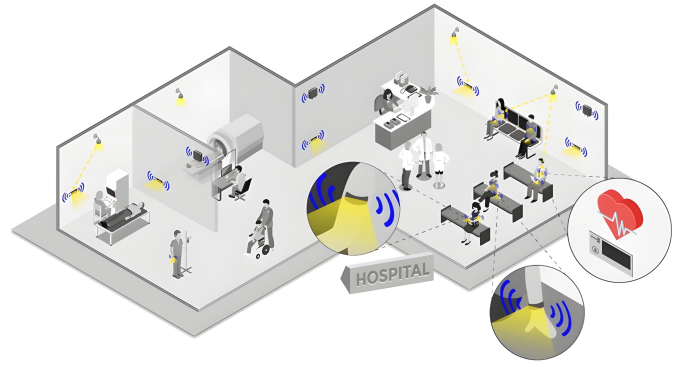


**FIGURE 1.** Illustration of a hybrid RF and OWC deployment in a hospital environment. RF ensures broad coverage and mobility for staff and patient monitoring, while OWC provides secure, interference-free communication for critical areas such as operating rooms and diagnostic imaging [20].

namic availability, and the constrained energy budgets of IoT devices. This is especially difficult in low-power IoT networks where decisions must be made promptly and often under uncertainty due to incomplete or changing channel conditions. Despite the growing body of research on hybrid RF-OWC systems, to the best of our knowledge, addressing these resource allocation challenges holistically in hybrid RF-OWC IoT networks remains an open research question.

## B. Contribution

In this work, we aim to investigate the resource allocation challenges in a hybrid dual-band IoT network that utilizes RF and OWC technologies [18]. We first formulate the optimization problem as a Mixed-Integer Non-Linear Programming (MINLP) which captures the full nonlinear interactions among energy consumption, link availability, and scheduling decisions. The MINLP is then approximated as a MILP using standard linearization techniques. The optimization problem has two-fold objectives: 1) maximize the throughput across the network with respect to energy consumption and 2) minimize the average delivery-based AoI in the network. As direct minimization of the time-average AoI is known to be intractable in general multi-source, multi-destination networks [19] due to the coupling of scheduling decisions over time and across links, we adopt a tractable surrogate that minimizes the age of each update at its delivery instant. Moreover, the proposed design considers the resource allocation problem over coherence time windows, in which the channel is assumed quasi-static. This is particularly valid in low-mobility IoT indoor environments where devices and surroundings exhibit minimal variation. In such settings, the quasi-static nature of the environment allows for reliable short-term predictions of Signal-to-noise Ratio (SNR) over short durations (e.g., 500 ms) [21]–[24]. This formulation enables dynamic, context-aware band selection, allowing IoT devices to autonomously select between RF and OWC based on slowly varying channel-state measurements and network conditions within each coherence-time window.

This paper extends our previous work [1] by reformulating the optimization problem to include more realistic RF and optical channel models, device-level energy and communication constraints, and comprehensive performance evaluations to validate the scalability, generalizability, and practical feasibility for hybrid RF-OWC IoT networks. Moreover, deterministic optimization methods are highly sensitive to link SNR estimates because they require precise, real-time knowledge of link states to compute feasible and optimal allocations. Therefore, given the NP-hardness of hybrid RF-OWC resource allocation [25] and the unrealistic assumption of full system knowledge, this work proposes an alternative data-driven Dual-Graph Embedding with Transformer (DGET) architecture utilizing Graph Neural Networks (GNNs) [26] and Transformers [27]. We first model the IoT network as a time-series graph, where each snapshot represents the network’s state at a given time. The *input snapshots* consist of known network states, including initial devices’ energy levels, transmission schedules, and available communication links over coherence time. The *recorded snapshots* represent the same network as it evolves, reflecting updates in energy, link status, and message queues due to ongoing communications. They are constructed by solving the scheduling problem using optimization techniques, and they contain ground truth values for the network changes.

The design of DGET is driven by the intrinsic characteristics of hybrid RF-OWC wireless networks, in which link relevance is governed by physical-layer factors such as visibility, blockage, interference, and device energy states, and where reliable observability is typically limited to a subset of known network snapshots. DGET explicitly exploits this asymmetry by first processing input snapshots through a transductive GNN [28], which learns fine-grained graph embeddings that capture both local and global structural patterns from the known network topology. These transductive embeddings are tailored to the hybrid RF-OWC IoT setting by jointly encoding device-level attributes (e.g., initial energy states) and edge-level features (e.g., RF-OWC link availability and scheduled transmissions), thereby enforcing stable structural priors and enabling attention mechanisms to identify physically meaningful neighbor-importance patterns across heterogeneous links, as supported by prior studies on fully observed graphs [29]. While this transductive stage yields optimized and consistent representations for observed network states, it is inherently limited in capturing instantaneous and evolving dynamics induced by time-varying conditions such as energy depletion, queue evolution, and adaptive scheduling decisions. This limitation is particularly critical in dynamic IoT environments, where device states, channel conditions, and scheduling queues change continuously as communication unfolds. To address this limitation, DGET incorporates an inductive GNN [30] that operates on top of the transductive embeddings, refining them by integrating decision-level information from recorded snapshots, including selected links, scheduling outcomes,

and energy updates. It learns an aggregation function that can generalize across graphs and also preserve the structure and reinforce the learned relationships obtained from the transductive embeddings through attention on the recorded snapshots. It is designed to promote knowledge transfer from the known snapshots seen during training through a domain adaptation mechanism, guided by a consistency loss aligning reconstructed embeddings with recorded graphs.

The proposed DGET model is trained using a multi-task learning framework. As the first task aligns reconstructed inductive embeddings with the ground truth recorded graphs, the second task performs communication link type classification using a Transformer-based architecture with a supervised learning setup. The Transformer’s attention mechanism on the resultant inductive embeddings enables global aggregation of these embeddings and reasoning over spatially distant devices and over multiple network snapshots, allowing the model to identify cross-device and temporal correlations in the IoT network to predict the optimal communication technology for each link. The supervised learning setup is motivated by the availability of high-quality optimal scheduling labels obtained from solving the MILP formulation across multiple network realizations, which further guide the DGET model towards learning physically consistent mappings between network states and scheduling decisions. This multi-task learning approach, designed for the hybrid RF-OWC IoT environment, allows DGET to simultaneously optimize two coupled tasks; aligning the embeddings reconstruction to the ground truth recorded graph and also improving the accuracy of link prediction.

The main contributions<sup>1</sup> in this paper can be summarized as follows:

- We present a system formulation for a hybrid RF-OWC network and formulate a constrained MINLP optimization problem, approximated as a MILP, that seeks to maximize the overall throughput of the network while taking into account the energy consumption and the delivery-based AoI.
- We introduce the DGET framework that combines two GNN components with a Transformer encoder to solve the resource allocation problem with lower overhead compared to solving the MILP problem. The transductive GNN learns fixed structural patterns from the known IoT network topology, while the inductive GNN generalizes these embeddings to temporally evolved configurations of the IoT network, capturing changes in energy, queue states, and link dynamics. A Transformer-based encoder applies self-attention to model complex dependencies and global relationships on the inductive GNN embeddings to predict active links and their corresponding transmission technology.

<sup>1</sup>The code for this paper has been made open source and can be accessed here: <https://github.com/aymenhamrouni/DGET-Dual-Graph-Embedding-Transformer-for-Hybrid-RF-OWC-IoT-Networks>

gies. The entire model is trained end-to-end using a multi-task learning framework with two coupled loss functions.

- We evaluate the performance of the hybrid RF-OWC network under varying conditions, including different network loads and sizes. Results demonstrate that the hybrid network can achieve up to 15% higher successful transmission rate and up to 20% reduction in Age-of-Information (AoI) compared to a standalone RF network. Under high network load scenarios, the RF-OWC configuration demonstrates improved energy efficiency. Furthermore, the proposed DGET framework achieves over 90% classification accuracy with up to 8x lower inference complexity compared to the optimization model and demonstrates robustness under partial system observability.

The remainder of this paper is organized as follows: Section II reviews the related work in the areas of hybrid RF-OWC communication and scheduling. In Section III, we describe the system model, detailing the channel characteristics, network architecture, and communication setup. Section IV formulates the optimal RF-OWC scheduling problem through a mathematical optimization framework. The proposed DGET framework is introduced in Section V, outlining its architecture and key components. Section VI presents the experimental evaluation used to assess the performance of our approach. Finally, Section VII concludes the paper and outlines directions for future research.

## II. Related Work

Given the growing interest in exploiting the complementary advantages of RF and OWC technologies, numerous studies have investigated dual-technology integration to enhance communication performance in various IoT scenarios. Tang et al. [31] investigated the resource allocation optimization for indoor hybrid RF-OWC systems. They formulated an optimization problem to maximize the minimum data collection rate across all IoT devices within the given time period. Fakirah et al. [32] investigated the integration of Visible Light Communication (VLC) with RF systems by using hybrid access points to facilitate seamless information exchange between vehicles and roadside units in a vehicle-to-infrastructure mode. Obeed et al. [33] proposed an iterative optimization-based algorithm for load balancing and power allocation in a hybrid RF-OWC system, consisting of a single RF access point and multiple OWC access points. Xiao et al. [34] examined a hybrid downlink system combining VLC and RF with a cognitive-based resource allocation policy to optimize network performance. Guo et al. [35] explored a relay-assisted network designed for simultaneous wireless information and power transfer, leveraging hybrid VLC-RF communication where a light-emitting diode access point serves multiple users engaged in both information exchange and energy harvesting. Alenezi et al. [36] proposed a Reinforcement Learning (RL) algorithm for the hybrid WiFi-

VLC scheduling problem, designed to operate on the WiFi side with the goal of maximizing throughput. Khalili et al. [37] presented a multi-attribute decision-making framework to manage handovers in RF-OWC heterogeneous networks, systematically evaluating APs under criteria including handover cost, data-rate demand vs. achievable rate, and capacity utilization. Collectively, these works underscore a crucial insight: RF alone faces spectrum congestion, interference, and coverage limitations, whereas OWC (or VLC) offers high capacity, unlicensed spectrum access, and improved security but suffers from line-of-sight and mobility constraints. Thus, dual-technology access becomes necessary to exploit their complementary strengths and meet the heterogeneous demands of dynamic IoT networks.

GNNs have been adopted in IoT networks [38]–[40], and recently in wireless communications networks [41], as they can effectively exploit domain knowledge [41], [42], i.e., the graph topology in wireless communications. Suarez-Varela et al. [43] highlighted the use of GNNs for the modeling, control, and management of communication networks. Shen et al. [26] demonstrated that GNNs can achieve near-optimal performance in wireless networks with fewer training samples compared to traditional neural networks. Yang et al. [41] proposed a GNN-based framework for optimizing wireless network performance, utilizing wireless interference graphs. Cheng et al. [44] proposed a model for resource allocation in heterogeneous D2D networks, addressing the limitations of traditional GNNs that often ignore graph devices' features and edges' features. Eisen et al. [45] addressed the resource allocation in wireless networks through a model-free approach using Random Edge Graph Neural Networks (REGNNs) that operate over interference-induced random graphs. Chen et al. [46] proposed a supervised GNN framework for device-to-device (D2D) resource allocation in wireless IoT networks, where communication links are represented as graph nodes and interference as edges. Zhao et al. [47] addressed distributed link scheduling in wireless networks by formulating it as a Maximum Weighted Independent Set (MWIS) problem, which is NP-hard. They proposed a graph convolutional network (GCN)-based approach that learns topology-aware graph node embeddings to improve greedy scheduling methods.

Existing studies on hybrid RF-OWC networks primarily use optimization methods that are computationally intensive. Moreover, they largely neglect information freshness metrics like AoI. While Graph Neural Networks have demonstrated efficacy in wireless resource management, their application to hybrid RF-OWC resource allocation, particularly when formulated as a classification problem incorporating device energy, packet requirements, and link quality, remains unexplored. In this work, we aim to address this research gap.

## III. System Model

In this section, we introduce the system model, represented by the network setup, channel model, and data commu-

TABLE 1. Main notations and their descriptions.

Notations	Descriptions
$\mathcal{N}_d$	Set of IoT nodes
$\mathcal{N}_{AP}$	Set of APs
$\mathcal{N}$	Total set of devices, $\mathcal{N}_d \cup \mathcal{N}_{AP}$
$\mathcal{T}$	Set of discrete time steps
$\mathcal{M}$	Set of communication technologies
$\xi_i$	Energy level of device $i$
$\xi_s^m, \xi_r^m$	Energy to transmit/receive a message using technology $m$
$\Phi_{i,j}$	Collection of valid time steps of messages from $i$ to $j$
$\phi_{i,j}^{f,l}$	Valid time steps of message $f$ of type $l$ from $i$ to $j$
$(\phi_{i,j}^{f,l})_s, (\phi_{i,j}^{f,l})_e$	Generation and discard time steps of message $f$ with type $l$ from $i$ to $j$
$\Gamma_{i,j}^f$	Number of packets in message $f$ from $i$ to $j$
$\mathbf{V}$	Visibility matrix for communication technologies
$x_{i,j,m,k}$	Binary value indicating transmitter, receiver, technology, and time step $k$
$\delta_{i,j,f}$	Time between generation and receipt of message $f$
$\tilde{y}_{i,j,m,f,k}$	Number of transmitted packets of message $f$ using technology $m$ at time $k$
$\mathbf{v}_i^I, \mathbf{v}_i^R$	Input and Recorded feature vector of device $i$
$\mathbf{e}_{ij}^I, \mathbf{e}_{ij}^R$	Input and Recorded edge feature from $i$ to $j$
$\mathcal{E}_t$	Set of allowed communication technology
$\mathcal{E}_c, \mathcal{E}'_c$	Set of initial and augmented communication status
$\mathcal{G}_k^I, \mathcal{G}_k^R$	Input and recorded graphs at time $k$

nication. For clarity, we provide the main notation used throughout the paper in Table 1.

### A. Network Setup

We consider a hybrid IoT network consisting of access points (APs) and nodes that can communicate through RF and OWC links. We assume that nodes communicate with APs using either OWC or RF, whereas only RF is used for inter-node communication. RF transmissions are assumed to happen in pre-assigned time slots using Time Division Multiple Access (TDMA), ensuring no two devices transmit simultaneously over the same channel. Moreover, we suppose that OWC uses tightly focused beams of visible or infrared light, which are inherently directional. Therefore, each device pair can establish either a LoS RF-OWC link or rely on a quasi-LoS RF link, minimizing inter-device interference. The system model with an RF-OWC hybrid configuration is illustrated in Fig. 2 with different IoT nodes transmitting multiple types of application data, such as sensor readings, status updates, and alarm messages.

Let  $\mathcal{N}_d$  be the index set of IoT nodes and  $\mathcal{N}_{AP}$  be the index set of APs in the system. The index set of total

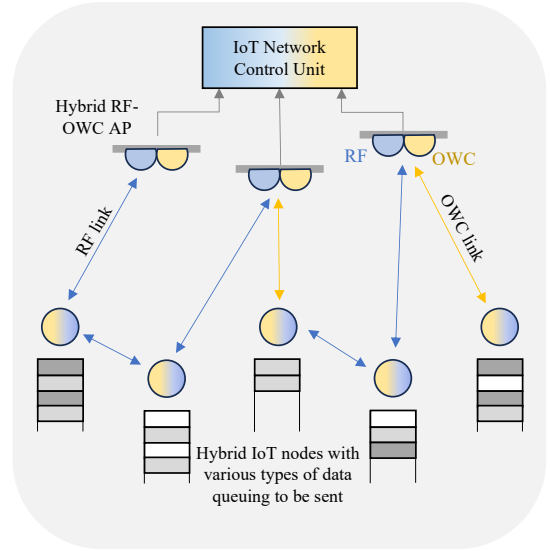


FIGURE 2. A visualization of the RF-OWC model showing a hybrid RF-OWC network exchanging different types of applications' data.

devices<sup>2</sup> in the network is denoted by  $\mathcal{N} = \mathcal{N}_d \cup \mathcal{N}_{AP}$ , with  $\mathcal{N}_d \cap \mathcal{N}_{AP} = \emptyset$ . Let  $\mathcal{M}$  be the set of possible communication technologies. In the network configuration considered,  $\mathcal{M} = \{0, 1\}$  with  $m = 0, m \in \mathcal{M}$  representing RF and  $m = 1, m \in \mathcal{M}$  denoting OWC. Let  $\mathcal{L}$  be the set of different data types in the system. For example, in the case of a healthcare scenario, where IoT sensors exchange two types of messages, e.g., heart rates and oxygen levels; we have  $|\mathcal{L}| = 2$ . We model the communication in the network over time by an equal-length discrete time horizon  $\mathcal{T}$ , which reflects the channel coherence time. This horizon is segmented into time steps  $[1, 2, \dots, |\mathcal{T}|]$ , where each time step is a single time unit denoted by the scalar  $\tau$  (in seconds).

### B. Channel Model

The path loss,  $PL$ , in dB considered for an indoor RF channel [48] is given as:

$$PL[\text{dB}] = PL_0[\text{dB}] + 10\alpha \log_{10} \frac{d}{d_0} + \psi[\text{dB}], \quad (1)$$

where  $PL_0$  is the path loss at a reference distance  $d_0 = 1$  m from transmitter,  $\alpha$  is the path loss exponent,  $d$  is the distance between transmitter and receiver, and  $\psi$  is a log-normal shadow fading with zero mean and variance  $\sigma_\psi^2$ . Consequently, the received power accounting for both large-scale and small-scale fading effects is expressed as:

$$P_r^{\text{RF}} = P_t^{\text{RF}} G_t G_r 10^{-\frac{PL[\text{dB}]}{10}} |h|^2, \quad (2)$$

where  $P_t^{\text{RF}}$  is the transmitted power,  $G_t, G_r$  are the gains of the transmitter and receiver antennas. Here  $h$  is the small-

<sup>2</sup>Throughout this work, the term device collectively refers to both IoT nodes and APs.

scale Rician fading coefficient, given by [48]:

$$h = \underbrace{\sqrt{\frac{K}{1+K}} e^{j\gamma}}_{\text{LoS component}} + \underbrace{\sqrt{\frac{1}{1+K}} z}_{\text{NLoS component}},$$

where  $K$  is the Rician factor, representing the ratio of the power in the LoS component to the power in the NLoS components,  $\gamma \sim \mathcal{U}(0, 2\pi)$  being a uniformly distributed random variable for the LoS phase, and  $z \sim \mathcal{CN}(0, 1)$  is a complex Gaussian random variable representing the NLoS components. To characterize the quality of the RF communication signals, we rely on the SNR [48], which is given as:

$$SNR^{\text{RF}} = \frac{P_r^{\text{RF}}}{N_{\text{RF}}}, \quad (3)$$

where  $N_{\text{RF}} = k_B T B_{\text{RF}}$  represents the noise power. Here,  $B_{\text{RF}}$  is the RF bandwidth,  $k_B$  is the Boltzmann constant ( $1.38 \cdot 10^{-23}$  J/K) and  $T$  is the room temperature (in Kelvin). Given the time-varying nature of the wireless channel, we define  $SNR_{i,j,k}^{\text{RF}}$  as the SNR for the RF signals from device  $i$  and device  $j$  at time  $k$ . The achievable rate between any device pairs at time  $k$  is computed as  $C_{i,j,k}^{\text{RF}} = B_{\text{RF}} \log_2(1 + SNR_{i,j,k}^{\text{RF}})$ .

In LED-based OWC, the optical power received  $P_r^{\text{OWC}}$  is determined by the Lambertian radiation pattern of the LED, geometric attenuation, atmospheric loss, and receiver characteristics [49]. It is computed as follows:

$$P_r^{\text{OWC}} = \kappa P_t^{\text{OWC}} T_{\text{Opt}} \frac{(u+1) A_{\text{Rec}} \cos^u(\theta) \cos(\phi)}{2\pi d^2}, \quad (4)$$

with  $\kappa$  is a coefficient  $\in (0, 1]$  that models power splitting between actual data modulation and lighting,  $P_t^{\text{OWC}}$  is the transmitted optical power in Watts (W),  $T_{\text{Opt}}$  is the total optical efficiency (lens/filter losses),  $u$  is the Lambertian order,  $A_{\text{Rec}}$  is the photodiode effective area (in meters<sup>2</sup>),  $\theta$  is the LED irradiance angle at the transmitter,  $\phi$  is the photodiode incidence angle at the receiver, and  $d$  is the link distance (in meters). The photodiode converts  $P_r^{\text{OWC}}$  to electrical current via responsivity  $\eta_r$  (Ampere/Watt):

$$I_r = \eta_r P_r^{\text{OWC}}. \quad (5)$$

The SNR formula can then be expressed as follows [50]:

$$\begin{aligned} SNR^{\text{OWC}} &= \frac{I_r^2}{N_{\text{shot}}^2 + N_{\text{thermal}}^2} \\ &= \frac{(\eta_r P_r^{\text{OWC}})^2}{2q(\eta_r P_r^{\text{OWC}} + \eta_r P_n) B_{\text{OWC}} + \frac{4k_B T}{R_L} B_{\text{OWC}}}, \end{aligned} \quad (6)$$

where  $B_{\text{OWC}}$  is the OWC bandwidth and the shot noise is expressed as  $N_{\text{shot}} = \sqrt{2q(I_r + I_n) B_{\text{OWC}}}$  with  $q$  the Electron charge ( $1.6 \cdot 10^{-19}$ C) and  $I_n = \eta_r P_n$  is the background light-induced current from the ambient light's noise power  $P_n$ . The thermal noise is also expressed as  $N_{\text{thermal}} = \sqrt{\frac{4k_B T}{R_L} B_{\text{OWC}}}$  with  $R_L$  being the load resistance ( $\Omega$ ). Similarly as RF, we define  $SNR_{i,j,k}^{\text{OWC}}$  from device  $i$  and device  $j$  at time  $k$ . The achievable rate for

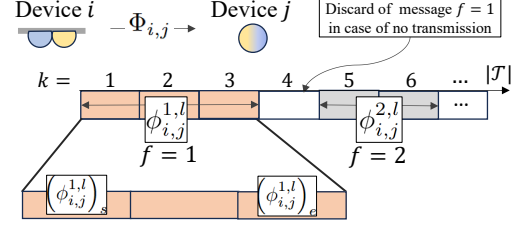


FIGURE 3. Illustration of the communication model and the lifespan of messages.

OWC between a transmitter  $i$  and a receiver  $j$  at time  $k$  is  $C_{i,j,k}^{\text{OWC}} = B_{\text{OWC}} \log_2(1 + SNR_{i,j,k}^{\text{OWC}})$ .

### C. Communication Setup

In order to capture the quasi-stationary indoor communication channel, we define a 4-D visibility matrix  $\mathbf{V}$ , with dimension  $|\mathcal{N}| \times |\mathcal{N}| \times |\mathcal{T}| \times |\mathcal{M}|$ , and where its elements are the scalar  $SNR_{i,j,k}^m$ . This visibility matrix governs the communication flow between any two devices in the network. Given that IoT nodes cannot communicate with each other using OWC, we represent this by setting  $SNR_{i,j,k}^1 = -\infty, \forall (i, j) \in \mathcal{N}_d \times \mathcal{N}_d, \forall k \in \mathcal{T}$ . Similarly, as communications between APs are assumed to be done on a separate dedicated medium,  $SNR_{i,j,k}^m = -\infty, \forall (i, j) \in \mathcal{N}_{AP} \times \mathcal{N}_{AP}, \forall m \in \mathcal{M}, \forall k \in \mathcal{T}$ . To model the communication over time, we introduce the matrix  $\mathbf{P}$ , which defines the communication schedule between any two devices at any given time. The elements of this matrix,  $\rho_{i,j}^k$ , are binary values, where  $\rho_{i,j}^k = 1$  indicates that communication will occur between devices  $i$  and  $j$  at time step  $k$ , and  $\rho_{i,j}^k = 0$  otherwise.

In our communication model, data are transmitted between devices in the form of messages, where each message is composed of a series of independent packets. A packet represents a smaller unit of data within a message, and the size of each packet in bits is denoted by  $s_p$ .

To define the lifespan for generated messages, we denote  $\Phi_{i,j} = \{\phi_{i,j}^{1,l}, \phi_{i,j}^{2,l}, \dots, \phi_{i,j}^{|\Phi_{i,j}|,l}\}$  as the collection of valid time steps for the messages to be sent from the device  $i$  to the device  $j$ . In this sense,  $\phi_{i,j}^{1,l}$  represents the set of valid time steps corresponding to the first message in the queue that needs to be sent from device  $i$  to device  $j$ . For instance, assume we have two messages to be sent from device  $i$  to device  $j$  with  $\Phi_{i,j} = \{\{1, 2, 3\}, \{5, 6\}\}$ . This implies that the first and the second messages can only be communicated during one of the time steps  $\{1, 2, 3\}$  and  $\{5, 6\}$ , respectively, before they get discarded. An illustrative example is shown in Fig. 3. Packets belonging to a message in  $\Phi_{i,j}$  must be sent at most once during their validity window represented by the message generation time and discard time (e.g., 1 is the generation time of the first message in the previous example, while 4 is its discard time). The discard time represents the maximum time at which the packets of the message could be sent before they are considered aged. We denote  $(\phi_{i,j}^{1,l})_s$  as

the generation time of message  $f$  and  $\left(\phi_{i,j}^{1,l}\right)_e$  as its discard time. Intuitively, there is no overlap between the time steps of any two distinct messages for a given device. In other words,  $\phi_{i,j}^{f,l} \cap \phi_{i,j}^{f',l} = \emptyset, \forall f \neq f'$ . In addition, we assume that each generated message can have a single type of data. Hence,  $\phi_{i,j}^{f,l} \cap \phi_{i,j}^{f',l'} = \emptyset, \forall l \neq l'$ . Let  $\Gamma_{i,j}^f \in \mathbb{Z}_{>0}, f \in [1, \dots, |\Phi_{i,j}|]$  represent the amount of data included in message  $f$  in terms of number of unit packet size  $s_p$ .

Each IoT device  $i \in \mathcal{N}$  is assigned a total energy budget  $\xi_i$ . The energy (joules/bit) for transmitting or receiving between device  $i$  and device  $j$  using RF is computed as follows [48]:

$$\xi_s^{\text{RF}} = \frac{P_t^{\text{RF}}}{C^{\text{RF}}}, \quad \xi_r^{\text{RF}} = \frac{P_r^{\text{RF}}}{C^{\text{RF}}}. \quad (7)$$

The energy (joules/bit) for transmitting or receiving between device  $i$  and device  $j$  using OWC is computed as follows [51]:

$$\xi_s^{\text{OWC}} = \frac{P_t^{\text{OWC}}}{\eta_c C^{\text{OWC}}}, \quad \xi_r^{\text{OWC}} = \frac{I_r V_{\text{bias}}}{C^{\text{OWC}}}, \quad (8)$$

where  $\eta_c$  is the electrical-to-optical conversion efficiency and  $V_{\text{bias}}$  is the bias voltage of the photodetector during reception.

#### IV. Optimal RF-OWC Scheduling

This section defines the optimization problem in RF-OWC IoT settings by outlining the decision variables, the constraints, and the overall objective function.

##### A. Decision Variables

In order to indicate the chosen 2-tuples (transmitter, receiver) and to keep track of assigned communication technology at each time step, we introduce the *main* binary decision variable  $x_{i,j,m,k}$  defined as follows:

$$x_{i,j,m,k} = \begin{cases} 1, & \text{if device } i \text{ transmits a message to device } j \\ & \text{using technology } m \text{ at time step } k, \\ 0, & \text{otherwise,} \end{cases} \quad \forall (i,j) \in \mathcal{N} \times \mathcal{N}, \forall m \in \mathcal{M}, \forall k \in \mathcal{T}. \quad (9)$$

Unless otherwise stated, indices  $i, j$  denote devices,  $k$  denotes the time step, and  $m$  denotes the communication technology. To keep track of which technology device  $i$  is using at time step  $k$ , we introduce a continuous *endogenous* binary variable  $s_{i,k}$ , which is 0 if device  $i$  is using RF, and 1 if it is using OWC. Throughout this paper, we assume that the receiver's queuing delay, propagation delay, and processing delay are negligible and focus solely on the transmitter's queuing delay and transmission delay. The transmission delay is treated as the unit of time for both RF and OWC.

##### B. Constraints

###### 1) Scheduling Constraints

To ensure that each IoT device within the network can communicate with at most one other device and use either RF or OWC at each time step, we include the following

constraints:

$$\begin{aligned} \sum_{j \in \mathcal{N}} \sum_{m \in \mathcal{M}} x_{i,j,m,k} &\leq 1, \quad \forall i, \forall k \\ \sum_{i \in \mathcal{N}} \sum_{m \in \mathcal{M}} x_{i,j,m,k} &\leq 1, \quad \forall j, \forall k \end{aligned} \quad (10)$$

Any device  $j$  engaged in communicating at a given time step with another device  $i$  cannot simultaneously communicate with another device  $j'$ . This is set by the following constraints:

$$x_{i,j,m,k} + x_{j,j',m',k} \leq 1, \quad \forall (i,j,j') \in \mathcal{N} \times \mathcal{N} \times \mathcal{N}, \\ \forall (m,m') \in \mathcal{M} \times \mathcal{M}, \forall k \in \mathcal{T} \quad (11)$$

In the event of no communication during the time step  $k$ , the value  $s_{i,k}$  is equal to  $s_{i,k-1}$ . Initially, every device starts with  $s_{i,-1} = 0$  (i.e., RF initialization). The constraints are then written as:

$$s_{j,k} = \begin{cases} m, & \sum_{i \in \mathcal{N}} (x_{i,j,m,k} + x_{j,i,m,k}) = 1 \\ 1, & \sum_{m \in \mathcal{M}} \sum_{i \in \mathcal{N}} (x_{i,j,m,k} + x_{j,i,m,k}) = 0 \wedge s_{j,k-1} = 1 \\ 0, & \sum_{m \in \mathcal{M}} \sum_{i \in \mathcal{N}} (x_{i,j,m,k} + x_{j,i,m,k}) = 0 \wedge s_{j,k-1} = 0 \end{cases} \quad (12)$$

$$\forall j, \forall m, \forall k,$$

with  $\wedge$  being the logical AND operation. To avoid frequent technology switching between RF and OWC, we introduce the following constraints:

$$\sum_{k \in \mathcal{T}} |s_{j,k} - s_{j,k-1}| \leq \Omega, \forall j, \quad (13)$$

with  $\Omega$  is a custom threshold that defines the maximum switching rate for each device in the network. The highest value of  $\Omega$  is  $\frac{|\mathcal{T}|}{2}$ , which in this case means that each device in the network is allowed to consecutively alternate between RF and OWC. We should note that these constraints can be integrated with the previous constraints to incur an energy loss or a delay to the network in case of frequent switching between technologies.

###### 2) Traffic and Message Validity

To ensure that communication between devices can happen only when there is an actual message to be transmitted, we add the following constraints:

$$\sum_{m \in \mathcal{M}} x_{i,j,m,k} \leq \rho_{i,j}^k, \quad \forall i, j, \forall k. \quad (14)$$

The following constraints in (15) extract the AoI at the delivery instant and are computed using the relative time offset within the valid window of a message sent from device  $i$  to device  $j$ . If the message was sent successfully at the  $k$ -th time step, this duration of elapsed time is  $k - \left(\phi_{i,j}^{f,l}\right)_s + 1$  between the current time and the generation time step of message  $f$  and counting the unit transmission delay. In the absence of transmission,  $\delta_{i,j,f}$  is set to an upper bound  $\chi$  that represents a strict bound on the time duration of the longest message in the system (i.e.,  $\max(|\phi_{i,j}^{f,l}|), f \in [1, \dots, |\Phi_{i,j}|]$ ,

$l \in \mathcal{L}$ ). These constraints are written as follows:

$$\delta_{i,j,f} = \begin{cases} k - \left(\phi_{i,j}^{f,l}\right)_s + 1, & \sum_{m \in \mathcal{M}} x_{i,j,m,k} = 1 \\ \chi, & \sum_{m \in \mathcal{M}} x_{i,j,m,k} = 0 \end{cases} \quad (15)$$

$$\forall k \in \phi_{i,j}^{f,l}, \forall l, \forall f \in \{1, \dots, |\Phi_{i,j}|\}, \forall i, j.$$

Any device in the system can transmit multiple messages to a single receiver, and each of these messages can have different types of data. As each message has a duration of validity over several time steps, as discussed in the previous section, we impose the following constraints so that packets within the message, regardless of the latter's data type, can be sent at most once within their valid time window:

$$\sum_{m \in \mathcal{M}} \sum_{k \in \phi_{i,j}^{f,l}} x_{i,j,m,k} \leq 1, \quad \forall i, j, \forall f \in [1, \dots, |\Phi_{i,j}|], \forall l \in \mathcal{L} \quad (16)$$

where  $\phi_{i,j}^{f,l}$  represents the valid time slots of message  $f$  with data type  $l$  that should be sent from device  $i$  to device  $j$ .

In our network setup, message size  $\Gamma_{i,j}^f$  is defined as a positive integer, representing the number of packets  $s_p$  in message  $f$ . If device  $i$  has more than one unit of a packet to transmit to device  $j$  (i.e.,  $\Gamma_{i,j}^f > 1$  for  $f \in [1, \dots, |\Phi_{i,j}|]$ ), it may either transmit all the packets within that message, none, or a part of that message. In this design, all packets can be transmitted within their corresponding message's validity window. However, not all packets need to be sent; a subset of the packets can be transmitted at any given time. For example, in large-scale IoT networks where an IoT node collects air quality data from different nearby locations, an IoT device has a limited time window to transmit the data. During this time window, the device may transmit all 20 packets, only 3 packets, or none at all if the device is unable to transmit due to network congestion. To model such behavior, we introduce the following constraints:

$$0 \leq x_{i,j,m,k} \left( \Gamma_{i,j}^f - y_{i,j,f} \right) \leq \frac{C_{i,j,k}^m}{s_p} \tau, \quad (17)$$

$$\forall k \in \phi_{i,j}^{f,l}, \forall l, \forall m, \forall f \in \{1, \dots, |\Phi_{i,j}|\}, \forall i, j,$$

where  $y_{i,j,f}$  is an *endogenous* integer variable representing the non-communicated number of packets. It is greater than or equal to zero and less than the maximum number of packets per message  $\bar{\sigma}$  (e.g.,  $\bar{\sigma} = \max(\Gamma_{i,j}^f)$ ). We note here that the non-communicated packets during a time step  $k$  can still be communicated at  $k' > k$  using either available communication technology as long as the packets did not reach their discard time. We have a product of two variables, the *main* decision variables  $x_{i,j,m,k}$  and the *endogenous* variable  $y_{i,j,f}$ . We linearize the product of binary and continuous variables in (17) using the McCormick [52] linearization by introducing a new *auxiliary* non-negative integer variable denoted by  $\tilde{y}_{i,j,m,f,k}$  such that  $\tilde{y}_{i,j,m,f,k} = x_{i,j,m,k} \left( \Gamma_{i,j}^f - y_{i,j,f} \right)$ .

### 3) Physical and Link Feasibility

Despite the inherent assumption that can be made in the communication matrix  $\mathbf{P}$  (or in  $\mathbf{V}^m$ ) that denies self-communication, the following constraint explicitly enforces that rule within the optimization model.

$$x_{i,i,m,k} = 0, \quad \forall i, \forall m, \forall k \quad (18)$$

If a device opts to communicate using a communication technology, the communication must be possible. To this end, we set a pre-defined threshold  $SNR_{min}^m, m \in \mathcal{M}$  that determines the minimum SNR value that must be satisfied by the visibility matrix  $\mathbf{V}^m$  for the communication to be considered successful, which is represented by:

$$SNR_{min}^m - U(1 - x_{i,j,m,k}) \leq SNR_{i,j,k}^m, \quad \forall i, j, \forall m, \forall k \quad (19)$$

with  $U$  a large number that accounts for the SNR values less than  $SNR_{min}^m$ .

In order to prevent devices from exceeding the energy budget allocated to their communication technology, we introduce the following constraint:

$$\sum_{m \in \mathcal{M}} \sum_{j \in \mathcal{N}} \sum_{k \in \phi_{i,j}^{f,l}} \left[ \tilde{y}_{i,j,m,f,k} \xi_s^m + \tilde{y}_{j,i,m,f,k} \xi_r^m \right] \leq \frac{\xi_i}{s_p}, \quad \forall i. \quad (20)$$

The previous conditional constraints (12), (13), and (15) are inherently nonlinear, but we can approximate and enforce these conditions in linear programming by using the Big-M method [53].

### C. Problem Formulation

Given a hybrid RF-OWC IoT network with devices engaged in exchanging messages over discrete time steps, the objective function is designed to maximize the overall throughput in the network with respect to energy consumption while minimizing the average packet delivery. Rather than optimizing the time-average AoI state process, which is intractable in multi-source networks, we minimize the age of each update at its delivery time  $\delta_{i,j,f}$ . This surrogate eliminates temporal state coupling and yields an additive, tractable objective.

This bi-objective optimization can be formulated as follows:

$$\text{P1: } \min_{x, \delta, \tilde{y}} \alpha_1 \frac{\sum_{i,j,f} \delta_{i,j,f}}{S_1} - \alpha_2 \frac{\sum_{i,j,m,f,k} \frac{\tilde{y}_{i,j,m,f,k}}{(\xi_r^m + \xi_s^m)}}{S_2},$$

subject to: (10) – (20).

In (P1), the terms  $S_1$  and  $S_2$  are normalization coefficients that take the maximum possible value for each sub-objective. However, such normalization alone often proves insufficient as certain terms can disproportionately dominate the optimization process or cause solution saturation. This issue arises because each term has a different sensitivity to the input change, causing some to inherently carry more weight even when normalized. Therefore, to mitigate the scaling issue between the terms, we introduce the regularization factors  $\alpha_1$  and  $\alpha_2$ , where  $\sum_{i=1}^2 \alpha_i = 1$ .

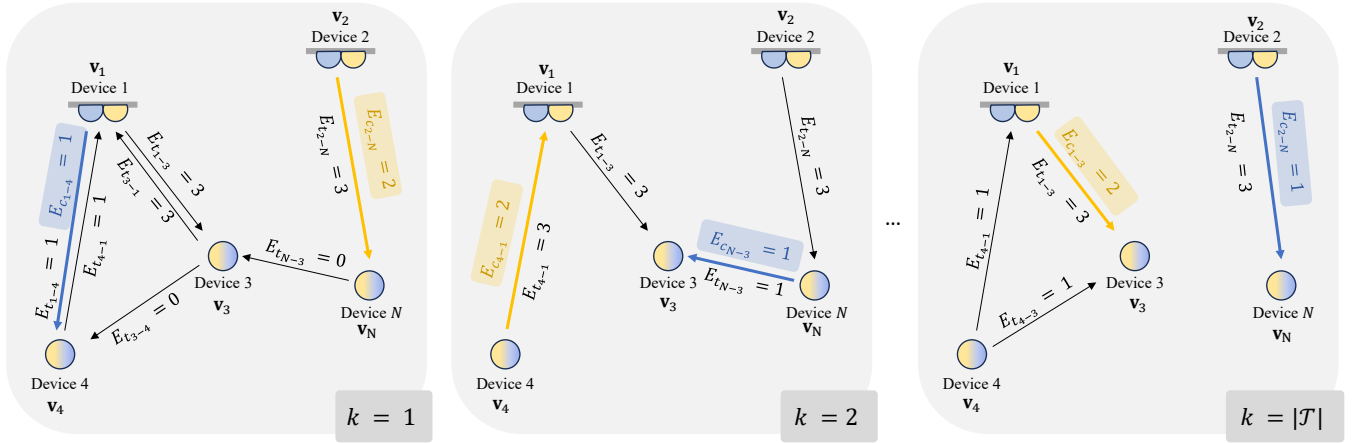


**FIGURE 4.** An example of a graph modeling for a network with  $N$  devices over a period of time  $\mathcal{T}$ .  $E_{t_{i-j}}$  represents the allowed communication links from device  $i$  to device  $j$ .  $E_{c_{i-j}}$ , on the other hand, represents the chosen communication technology for that link. For illustration, we have omitted some of the communication links that cannot be established from a device  $i$  to a device  $j$  to showcase the environment visibility (i.e.,  $E_{t_{i-j}} = 0$ ). The edges in yellow/blue represent the chosen links and their value (e.g.,  $E_{c_{2-3}} = 2$  refers to OWC) at each time  $k \in \mathcal{T}$ .

The initial formulation has nonlinear constraints (e.g., Eq. (15) & Eq. (12)) and a non-convex term (e.g., Eq. (17)) defining a conceptual MINLP. Applying the McCormick and Big-M reformulations yields an equivalent MILP, where the objective and all constraints are linear. Although the continuous relaxation is convex, the presence of binary variables makes the feasible region non-convex and the problem combinatorial. Such problems are known to be NP-hard [25]. State-of-the-art solvers, such as branch-and-bound or branch-and-cut [54], have a worst-case runtime that grows exponentially with a time complexity of  $\approx O\left[2^{(|\mathcal{N}|^2 \times |\mathcal{M}| \times |\mathcal{T}|)}\right]$ , which is computationally expensive for large-scale IoT networks. Nevertheless, the MILP formulation serves as a performance oracle to generate globally optimal scheduling labels and to benchmark the learning-based approach. In the next section, we introduce our model DGET that relies on graph embedding techniques along with the Transformer-based architectures to learn the devices' scheduling timetable and technology usage at each time with lower overhead.

## V. Proposed Graph Transformers Network for RF-OWC IoT Networks

In this section, we present the designed DGET framework for resource allocation in hybrid RF-OWC IoT networks. We begin the section with the graph modeling approach and explain how the hybrid RF-OWC IoT network is modeled into temporal snapshots. We then introduce the dual embedding framework via GNNs<sup>3</sup> and present the Transformer-based classifier that operates on the generated embeddings to enable resource allocation decisions. Finally, we detail the customized learning strategies that enhance model learning and prediction robustness.

<sup>3</sup>Readers that are not familiar with GNNs are encouraged to check [55]–[57].

### A. Graph Modeling

As an alternative to solving the computationally expensive problem (P1), the RF-OWC hybrid IoT network can be modeled as a temporal directed graph  $\mathcal{G}_k(\mathcal{V}, \mathcal{E}), k \in \mathcal{T}$ , where the vertices represent the total IoT devices (ie,  $|\mathcal{V}| = |\mathcal{N}|$ , including IoT nodes and APs) and the edges denote the hybrid communication links at any time step  $k \in \mathcal{T}$ . An example illustrating the concept is provided in Fig. 4. Since the graph is directed and self-loops are disallowed (i.e., a device cannot communicate with itself), the total number of potential edges is  $|\mathcal{E}| = |\mathcal{N}|(|\mathcal{N}| - 1)$ .

To capture the time-varying nature of the network, we define two types of time-series graph snapshots:  $\mathcal{G}_k^I(\mathcal{V}, \mathcal{E})$  and  $\mathcal{G}_k^R(\mathcal{V}, \mathcal{E})$ . The first graph,  $\mathcal{G}_k^I(\mathcal{V}, \mathcal{E})$ , which will be referred to as *input graph*, captures the state of the environment at time  $k$  and includes prior knowledge of the network including allowable communication technologies between devices, initial energy levels, and feasibility and quality of links. In contrast, the second graph,  $\mathcal{G}_k^R(\mathcal{V}, \mathcal{E})$ , which will be referred to as *recorded graph*, represents the resulting state of the system after communication activities have taken place. This graph reflects communication updates such as exchanged messages, link selections, and energy depletion resulting from actual communication activities. These states depend on the scheduling decisions made by solving the optimization problem formulated in Section IV.

For the input graph, each device  $i \in \mathcal{V}$  is associated with a feature vector  $\mathbf{v}_i^I$ , which encodes its type and local state information (e.g., available packet for transmission, initial energy level, energy per bit consumption, total outgoing packets, etc.). In the recorded graph, the devices' features are referred to as  $\mathbf{v}_i^R$ , which contain  $\mathbf{v}_i^I$  but also the parameters evolution over time to reflect communication decisions made at each step (e.g., energy reduction due to data transmission). Similarly, the input graph includes a link feature vector from device  $i$  to device  $j$ , denoted as  $\mathbf{e}_{i,j}^I$ . The latter includes the prior knowledge link-specific information, such

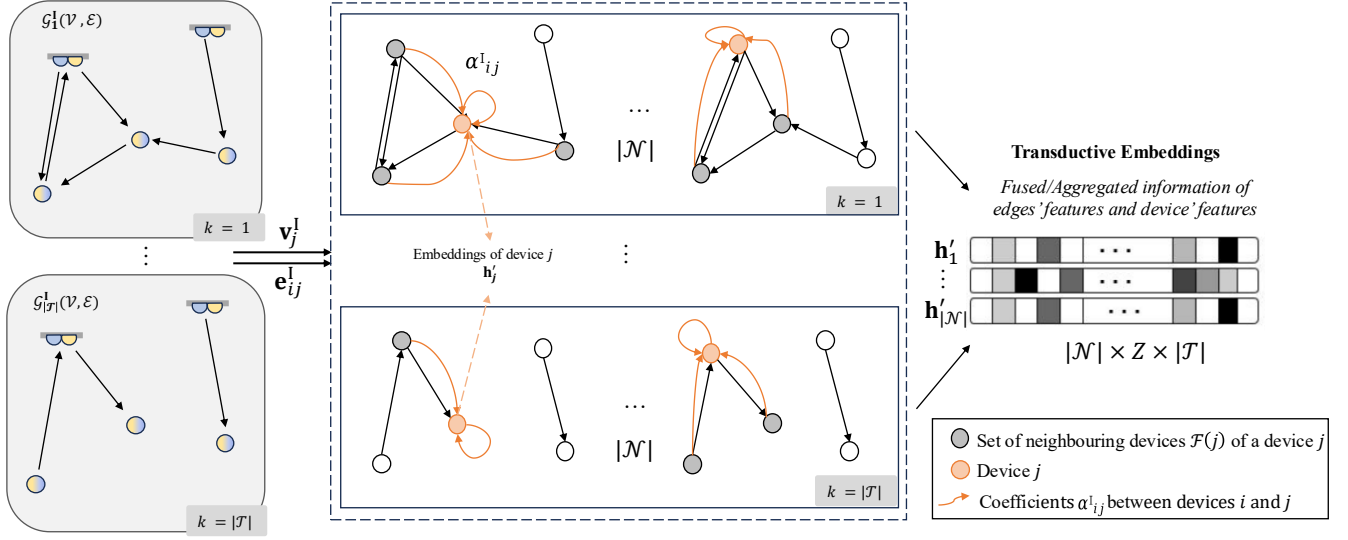


**FIGURE 5.** Visualization of device-link transductive embeddings from the network graph, resulting in a numerical representation for each device in the graph. Each temporal input graph  $\mathcal{G}_k^I(\mathcal{V}, \mathcal{E})$  is transformed into embeddings with a size  $|\mathcal{N}| \times Z$ , with  $Z$  the embedding dimension.

as the per-edge queue of messages, their types, and the link quality. The edges feature vector  $\mathbf{e}_{ij}^I$  contains the possible communication links  $\mathcal{E}_t = \{0, 1, 2, 3\}$ , which encodes the allowed communication technologies between two devices: 0 means no communication is possible, 1 allows only RF, 2 allows only OWC, and 3 allows either RF or OWC. This information is prior knowledge of both the input and the recorded graphs. In contrast, the recorded graph includes a link feature vector from device  $i$  to device  $j$ , denoted as  $\mathbf{e}_{ij}^R$ , which mirrors the input graph link feature and also includes the ground truth link status  $\mathcal{E}_c = \{0, 1, 2\}$ . The latter indicates the chosen communication links at a given time, with 0 denoting no communication occurred, 1 denoting RF communication was selected, and 2 denoting communication was via OWC. In this context, we note  $\mathcal{E}_{t,i,j}$  as the permissible communication technologies from device  $i$  to device  $j$ , while  $\mathcal{E}_{c,i,j}$  indicates the actual communication technology selected for transmission from device  $i$  to device  $j$ . Both the recorded device feature  $\mathbf{v}_i^R$  and the link's status  $\mathbf{e}_{ij}^R$  are obtained as a result of solving (P1) in Section IV and recording the network parameter evolution. By definition, the selected communication status  $c \in \mathcal{E}_c$  must satisfy  $c \leq f$  for any edge, with  $f \in \mathcal{E}_t$ , ensuring the chosen technology complies with the available link constraints.

This modeling allows us to shift the resource allocation problem in the IoT network to predicting the value of  $c \in \mathcal{E}_c$  for each pair  $i, i'$  in the graph  $\mathcal{G}_k^I(\mathcal{V}, \mathcal{E})$  at any given time step  $k \in \mathcal{T}$ . We reformulate the task as a classification problem acting on the input graph. Specifically, we aim to predict the appropriate communication status  $c \in \mathcal{E}_c$  for each edge in the input graph  $\mathcal{G}_k^I(\mathcal{V}, \mathcal{E})$  at each time step  $k$  by establishing a learning process from the information in the recorded graph. We encode topology, traffic availability, link feasibility, and pre-decision link quality on edges, with

static device priors on nodes. Known graphs contain only pre-decision information, while recorded graphs mirror those features and add post-decision information, such as energy changes and chosen technology.

### B. Device-Link Embedding using GNN

Once we build the time-series graphs  $\mathcal{G}_k^I(\mathcal{V}, \mathcal{E})$  and  $\mathcal{G}_k^R(\mathcal{V}, \mathcal{E})$ , we proceed with embedding the device and edges into a latent space using a two-stage GNN pipeline that combines transductive and inductive learning. The first stage applies a transductive GNN on the input graph  $\mathcal{G}_k^I(\mathcal{V}, \mathcal{E})$  to generate an initial set of devices' embeddings. The transductive GNN operates over fully observed training graphs and has access to the entire graph topology and feature distribution. This allows it to generate globally consistent and context-aware embeddings with local and global interactions present in the input graph. In the second stage, we employ an inductive GNN to enrich the transductive representation by learning decision patterns from the recorded graph  $\mathcal{G}_k^R(\mathcal{V}, \mathcal{E})$ , with the latter acting as a supervised representation. In other words, the inductive GNN maps the transductive embeddings into richer and semantically aligned embeddings that resemble those obtained from the recorded graph snapshots given by  $\mathcal{G}_k^R(\mathcal{V}, \mathcal{E})$ . The inductive GNN acts as a semantic enhancer to refine and enrich transductive embeddings by learning how to incorporate the information seen only during training, such as the actual communication decisions and energy updates.

The key goal for transductive GNN is to produce rich embeddings of the graph while incorporating the features of the devices and their relationships at specific points in time. Furthermore, we are interested in extracting network information from the vertices, i.e., devices, and also from the edges, i.e., links. Therefore, we propose to leverage a mixture of vertex-edge embedding for each step. The

mapping function from the graph to vectors is represented by a component that captures the vertices' features and the respective links with their features. Graph Attention Networks (GATs) [58] are particularly well-suited for this task, as their attention mechanism adaptively weighs the influence of neighboring IoT devices based on both their features and the type or quality of the connecting link [59]. In the transductive setting, where the full network snapshot is observable, attention enables the model to learn discriminative structural priors by emphasizing technologically relevant RF-OWC interactions, such as feasible OWC links or energy-efficient RF paths, while down-weighting less informative or infeasible connections. This is critical at the transductive stage, where the goal is to extract stable structural priors that reflect the topology of the network rather than treating all neighbors uniformly. Building on this, we extend the attention formulation to also incorporate edge attributes so that the model can differentiate between heterogeneous RF-OWC connections. We define the following aggregation score  $A_{ij}^I$  between two devices  $i$  and  $j$ :

$$A_{ij}^I = \sigma \left( \beta (\mathbf{e}_{ij}^I) \mathbf{a}^T \text{Conc} (\mathbf{W} \mathbf{v}_i^I, \mathbf{W} \mathbf{v}_j^I) \right), \quad (21)$$

$$\forall (i, j) \in \mathcal{N} \times \mathcal{N},$$

where  $\mathbf{v}_i^I$  and  $\mathbf{v}_j^I$  are the feature vectors of devices  $i$  and  $j$  from the input graph  $\mathcal{G}_k^I(\mathcal{V}, \mathcal{E})$ ,  $\mathbf{W}$  is a learnable weight matrix,  $\text{Conc}(\cdot)$  denotes the concatenation function,  $\mathbf{a}$  is also a learnable attention vector,  $\sigma$  is a nonlinear activation function, and  $\beta$  the Min-Max normalization. For ease of explanation, we have included a high-level visualization in Fig. 5 highlighting the transductive embedding process. The inclusion of the normalized  $E_{t_{ij}}$  ensures that the importance of the connection between devices  $i$  and  $j$ , described by the possible communication technology in this case, is adjusted according to the weight of the edge. Then, the normalized coefficient  $\alpha_{ij}^I$  for the input graph is computed via a softmax function:

$$\alpha_{ij}^I = \frac{\exp(A_{ij}^I)}{\sum_{n \in \mathcal{V}} \exp(A_{in}^I)}, \quad \forall (i, j) \in \mathcal{N} \times \mathcal{N}. \quad (22)$$

Finally, the updated feature vector for device  $i$  is computed as:

$$\mathbf{h}_i' = \sigma \left( \sum_{j \in \mathcal{F}(i)} \alpha_{ij}^I \mathbf{W}' \mathbf{v}_j^I \right), \quad \forall i \in \mathcal{N}, \quad (23)$$

where  $\mathcal{F}(i)$  the set of neighbor devices to  $i$  and  $\mathbf{W}'$  is a learnable weight matrix.

While GATs employ parameter sharing, allowing their attention weights to be reused across compatible graphs, this property alone does not ensure meaningful generalization in dynamic environments. In a purely transductive setting, the learned embeddings are optimized for a fixed and fully observed graph, capturing specific node features, link states, and connectivity patterns. As a result, when the network topology or device attributes (e.g., energy levels, queue lengths, or hybrid RF-OWC link conditions) evolve over time, these embeddings must be recomputed and cannot

directly transfer to unseen configurations. The inductive GNN in DGET addresses this limitation by learning a generalizable aggregation function that adapts the transductive embeddings to dynamically changing graphs. The inductive GNN first acts on the recorded graph  $\mathcal{G}_k^R(\mathcal{V}, \mathcal{E})$ , where the goal is to embed the recorded graph into a supervised representation. In other words, inductive embeddings learn to enrich and refine the transductive embeddings given by the input snapshots  $\mathcal{G}_k^I(\mathcal{V}, \mathcal{E})$  while relying on the recorded graph embedding  $\mathcal{G}_k^R(\mathcal{V}, \mathcal{E})$  to generalize beyond the transductive learned patterns. To achieve this, we draw inspiration from the GraphSAGE framework [57] and incorporate attention-based neighbor weighting with explicit edge features into the aggregation process. Unlike vanilla GraphSAGE, which aggregates only node embeddings, our inductive GNN design concatenates edge attributes through a skip connection and modulates neighbor contributions based on the known input states. The output of the inductive embedding at the layer  $p$  is denoted by  $\mathbf{o}_i^p$  and expressed as follows:

$$\mathbf{o}_i^p = \sigma \left( \sum_{j \in \mathcal{F}(i)} \alpha_{ij}^I \mathbf{W}^p \mathbf{o}_j^{p'} \right), \quad \forall i \in \mathcal{N},$$

$$\mathbf{o}_j^{p'} = \sigma \left( \mathbf{W}^{p'} \text{Agr} \left( \text{Conc}(\mathbf{o}_i^{p-1}, \mathbf{e}_{ji}^I) \right) \right), \quad \forall i \in \mathcal{F}(j), \quad (24)$$

where  $\mathbf{o}_j^{p-1}$  is the embedding of the device  $j$  in the  $p-1$  layer obtained by following the chain equation in (24),  $\text{Agr}(\cdot)$  is a general neighborhood aggregation function (e.g., mean, pooling, or LSTM-based), and both  $\mathbf{W}^p$  and  $\mathbf{W}^{p'}$  are learnable weight matrices for layer  $p$ . The initialization value of  $\mathbf{o}_j^0$  is obtained from the transductive embedding  $h_i'$ . The inductive GNN is also provided with the edges' features  $\mathbf{e}_{ji}^I$  through a skip connection, which acts as an informational anchor that ensures the updated devices' embeddings remain consistent with the link-level constraints defined in the input graph. The obtained final embedding size  $\mathbf{o}_i^p$  is  $|\mathcal{T}| \times Z$ , where the rows represent the time dimension and  $Z$  is the embedding dimension.

### C. Consistency Embeddings

In the previous section, we discussed how the input time-series graph  $\mathcal{G}_k^I(\mathcal{V}, \mathcal{E})$  is transformed to embeddings by encoding vertex features and edge attributes through a series of transductive and inductive GNNs. In this section, we explain the overall flow of the DGET framework. For clarity, we have included an illustration of the high-level architecture in Fig. 6.

The transductive GNN operates over fully observed graphs and has access to the entire graph topology and feature distribution from the input graph  $\mathcal{G}_k^I(\mathcal{V}, \mathcal{E})$ . These embeddings are rich in structural priors and capture local and global interactions present in the graph. Once the transductive GNN has generated embeddings from the input graph  $\mathcal{G}_k^I(\mathcal{V}, \mathcal{E})$ , we pass them to an inductive GNN in the subsequent layer. The inductive GNN focuses on generalizing from the learned embeddings by using local neighborhood aggregation, which

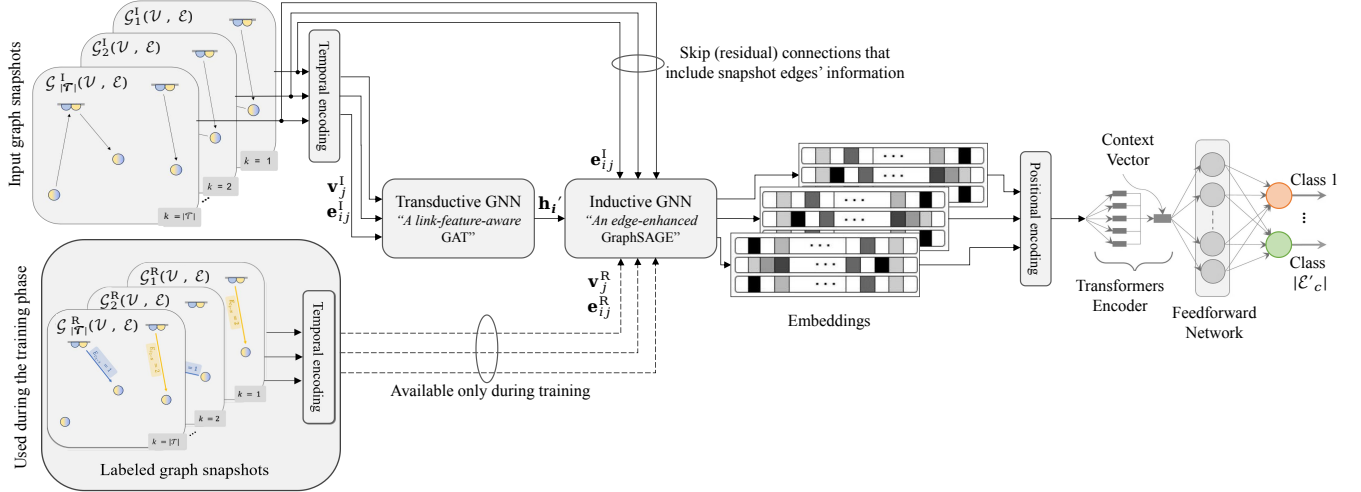


FIGURE 6. High-level architecture illustrating the different components of the DGET model.

allows it to capture temporal variations in device and link features during inference. The inductive model uses these initial embeddings from input snapshots as starting points, and through neighborhood-based computations, as shown in the previous subsection, it attempts to reconstruct or refine the embeddings by learning patterns from recorded snapshots  $\mathcal{G}_k^R(\mathcal{V}, \mathcal{E})$ .

To ensure these generated embeddings faithfully represent the ground-truth embeddings obtained from the recorded graph, we use a consistency loss function [60] that optimizes embedding accuracy by measuring the similarity between predicted embeddings from the input graph  $\mathcal{G}_k^I(\mathcal{V}, \mathcal{E})$  and the true embeddings  $\mathcal{G}_k^R(\mathcal{V}, \mathcal{E})$  from the recorded graph, which are only observed during training. The loss aims to align reconstructed embeddings with actual graph  $\mathcal{G}_k^R$  embeddings, minimizing error across time steps. This loss is represented as follows:

$$\mathbf{L}_{\text{consistency}} = \frac{1}{|\mathcal{N}|} \sum_{k \in \mathcal{T}, j \in \mathcal{V}} \|\mathbf{o}_j^p(k) - \mathbf{g}_j^p(k)\|_2^2, \quad (25)$$

where  $\mathbf{o}_j^p(k)$  is the final layer  $p$  predicted embedding for device  $j$  at time  $k$  and  $\mathbf{g}_j^p(k)$  is the final layer  $p$  true embedding for device  $j$  at time  $k$ . The true embeddings  $\mathbf{g}_j^p(k)$  are obtained using (24) acting on the recorded graph  $\mathcal{G}_k^R(\mathcal{V}, \mathcal{E})$ , therefore  $\mathbf{v}_i^R$  and  $\mathbf{e}_{ij}^R$ , and while recomputing the attention  $\alpha_{ij}^R$  to capture not only the initial state but also evolving node and link states. Attention is applied in both GNN stages but serves different purposes. The transductive GNN uses attention to encode stable structural importance from fully observed network snapshots. The inductive GNN re-applies attention to dynamically re-weight neighbors to adapt to dynamic changes in node energy, queue occupancy, link availability, and evolving connectivity patterns.

The consistency loss aims to minimize the discrepancy between the true observation, as a reference, on the recorded graph and the initial learned representation from the input graph by applying the mean squared error over all time steps.

To capture temporal information, we include a temporal encoding to each time snapshot graph, distinguishing each of their order in time. Temporal encoding enables the model to learn the evolution or time-based interactions between devices or edges. We should note that the inductive GNN operates in two modes. During training, the inductive GNN receives embeddings from the transductive GNN and the recorded graph with ground-truth outcomes. It learns to map the transductive embeddings to richer, semantically aligned embeddings using the consistency loss that penalizes discrepancies between reconstructed embeddings, from the input graph, and true embeddings, from the recorded graph. At inference, the inductive GNN uses only transductive embeddings and transforms these embeddings into enriched representations that capture the learned decision patterns and semantic structures.

#### D. Transformer-based Classification

To classify the communication links over time, we employ a Transformer-based classifier. This classifier utilizes an attention mechanism that operates on the sequence of devices' embeddings generated by the inductive GNN, allowing the model to weigh and select relevant information from each time step's embedding based on the relationships between embeddings across time. Positional encoding is applied to the generated graph embeddings to allow the Transformer-based classifier to be aware of the structure or relative position of embeddings input [27]. The Transformer block consists of multiple layers of multi-head self-attention and feedforward neural networks. The final layers are a feedforward neural network that yields, through a custom weighted loss function, the predicted class per link at time step  $k$ . In other words, the classifier outputs which devices will communicate with which devices and using which technology and at which time step  $k \in \mathcal{T}$ . The proposed DGET architecture leverages the strengths of both graph-based and sequence-based learning to provide a solution for predicting the scheduling of communication between the devices, along with the type

of medium used. The classification loss function is a negative log-likelihood loss represented as follows:

$$\mathbf{L}_{\text{classification}} = -\frac{1}{|\mathcal{N}|} \sum_{i \in \mathcal{N}} \log [p(y_i | x_i)], \quad (26)$$

where  $y_i$  is the true label for the  $i$ -th sample,  $x_i$  is the input for the  $i$ -th sample, and  $p(y_i | x_i)$  is the predicted probability of the true class for the  $i$ -th sample.

The final loss function for the overall architecture is represented as follows:

$$\mathbf{L} = \mathbf{L}_{\text{classification}} + \lambda \mathbf{L}_{\text{consistency}}, \quad (27)$$

with  $\lambda$  is a hyperparameter that controls the balance between the classification and consistency losses.

### E. Enhanced Learning Strategies and Post-processing

The graph  $\mathcal{G}_k^R(\mathcal{V}, \mathcal{E})$  has, at each time step, different  $|\mathcal{E}| = |\mathcal{N}|(|\mathcal{N}| - 1)$  edges that reflect the scheduling between the devices at each time. Therefore, at any time  $k \in \mathcal{T}$ , there can be at most  $\lfloor \frac{|\mathcal{N}|}{2} \rfloor$  non-zero class edges. This is because of the constraints that each time step, a device can communicate with only another device. Since  $\lfloor \frac{|\mathcal{N}|}{2} \rfloor \ll |\mathcal{N}|(|\mathcal{N}| - 1)$ , the vast majority of edge labels correspond to the no-communication class (i.e., class zero), resulting in a highly imbalanced class distribution. To address this challenge and improve classification performance, we propose a three-fold refinement and stability strategy.

The first fold involves augmenting the edge class space by correlating the communication class  $\mathcal{E}_c$  with the residual communication features  $\mathcal{E}_t$ , as shown in Fig. 6. Originally, the classifier outputs 3 classes (i.e.,  $\mathcal{E}_c = \{0, 1, 2\}$ ), representing the communication type (or no communication). However, by combining these with edge features  $\mathcal{E}_t = \{0, 1, 2, 3\}$ , we expand the space to 8 augmented classes  $\mathcal{E}'_c = \{0, 1, 2, 3, 4, 5, 6, 7\}$ . Each class in  $\mathcal{E}'_c$  reflects a joint event: the communication feasibility and the classifier's prediction. For example,  $\mathcal{E}'_c = 0$  means no communication was possible and correctly predicted as such;  $\mathcal{E}'_c = 1$  means communication via RF was possible but not predicted; and  $\mathcal{E}'_c = 2$  means communication via RF was both possible and predicted. This conditional labeling improves representation learning and balances the dataset by leveraging hidden semantic patterns in the edge features.

The second fold is to leverage a weighted loss function that gives more focus to under-represented classes (i.e., those that appear less frequently) and less importance to over-represented classes. The classification loss presented in (26) is therefore updated to a negative log-likelihood loss with weighted classes, and it is represented as follows:

$$\mathbf{L}_{\text{classification}} = -\frac{1}{|\mathcal{N}|} \sum_{i \in \mathcal{N}} \left( \sum_{c=0}^{C-1} w_c y_{ic} \log(\hat{y}_{ic}) W_{c, \hat{y}_i} \right), \quad (28)$$

where  $w_c$  is the inverse-frequency weight for class  $c$ ,  $y_{ic}$  is the true label indicator,  $\hat{y}_{ic}$  is the predicted probability for class  $c$ , and  $W_{c, \hat{y}_i}$  is the penalty weight that applies when the true class is  $c$  and the model predicts class  $\hat{y}_i$ .

TABLE 2. Simulation parameters for RF and OWC Systems.

Parameter	Value
<b>RF System</b>	
Bandwidth ( $B_{\text{RF}}$ )	2 MHz
Transmit Power ( $P_t^{\text{RF}}$ )	50 mW
Path Loss Exponent $\alpha$	3
$PL_0$	40 dB
$G_t = G_r$	5 dBi
RF SNR Threshold ( $\text{SNR}_{\text{min}}^0$ )	15 dB
<b>OWC System</b>	
Bandwidth ( $B_{\text{OWC}}$ )	1 GHz
Transmit Power ( $P_t^{\text{OWC}}$ )	5 W
Optical Transmission Coefficient ( $T_{\text{Opt.}}$ )	0.99
Lambertian order ( $u$ )	1
Illumination Coefficient ( $\kappa$ )	0.3
Incidence and Irradiance angles ( $\phi, \theta$ )	60°
Photodiode Effective Area ( $A_{\text{Rec}}$ )	0.0025 m <sup>2</sup>
Photodiode Responsivity ( $\eta_r$ )	0.6 A/W
Background Light power ( $P_n$ )	10 <sup>-9</sup> W
OWC SNR Threshold ( $\text{SNR}_{\text{min}}^1$ )	10 dB
<b>DGET Parameters</b>	
Number of GATs layers	64
Number of GATs Attention heads	4
Number of GraphSAGE layers	64
Embeddings Dimension of GraphSAGE	256
GraphSAGE Aggregation ( $Agg$ )	<i>mean()</i>
Transformer encoder layers	6
Number of Transformer attention heads	8
Transformer Embedding size	256
Dataset Split Train/Val-Test	80%:20%
Cross-Validation	Stratified 10-fold
Fold Train-Val	7:3
Epochs per Fold	70
Regularization	$L_2$
Dropout Rate	0.3
Weight Initialization	Xavier initialization
Activation Function ( $\sigma$ )	LeakyReLU
<b>System Parameters</b>	
Devices' Distance Range	$\mathcal{U}(3, 20)$ m
Sensitivity Coefficients $\alpha_1, \alpha_2$	0.35, 0.65

The matrix  $\mathbf{W}_{c, c'}$ , where  $c, c' \in \mathbb{R}^{C \times C}$  represents a penalty factor that adjusts the loss based on the predicted class to allow penalizing certain misclassifications. The weights  $w_c$  for each class are generally calculated based on the inverse of their frequency in the dataset.

The third fold incorporates a post-processing correction phase that ensures the feasibility of the predicted scheduling. After prediction, we perform a constraint check to detect violations (e.g., a device communicating with multiple others at the same time step  $k \in \mathcal{T}$ ). If infeasible predictions are found, we perform a top-2 accuracy search: the second-highest class from the classifier's output distribution is selected, and the feasibility is re-evaluated. The rationale is

that most errors occur between semantically adjacent classes (e.g.,  $\mathcal{E}'_c = 1$  vs.  $\mathcal{E}'_c = 2$ ), due to the structured residual encoding introduced by the augmented labels and class penalty design  $\mathbf{W}_{c,c'}$ . Indeed, this post-processing approach is more effective when the initial classifier solution results in more communication between devices than is permissible. Therefore, we adapt the weighted loss function in (28) to attribute high penalization to the nearby classes except for the classes that result in over-predicting. This leads to a powerful elimination of false positives and reduces the number of false negatives. After that, and to backtrack and eliminate non-allowed communication, we create a mapping matrix with the indices of the feasible set in the solution vector. Let this mapping be the matrix  $\mathbf{M}_p$  with size  $\frac{|\mathcal{N}|(|\mathcal{N}|-1)}{2}$  and  $(|\mathcal{N}|(|\mathcal{N}|-1)) - ((|\mathcal{N}|-2)(|\mathcal{N}|-3))$ . For clarity, we can take the example of a network of  $|\mathcal{N}| = 4$  devices. We have then  $|\mathcal{N}|(|\mathcal{N}|-1) = 12$  potential links between these devices. If we enumerate these links, we have the following arrangements:  $\{1-2, 1-3, 1-4, 2-1, 2-3, 2-4, 3-1, 3-2, 3-4, 4-1, 4-2, 4-3\}$ . The feasibility matrix has a size of  $6 \times 10$  with the rows representing the combination of three devices as  $\{1-2, 1-3, 1-4, 2-3, 2-4, 3-4\}$  and the columns representing the set for each pair of these devices that overlap (i.e., only one of these sets can communicate). In this case, the first column has all the pairs of devices that include device 1 and device 2 which is  $\{1-2, 1-3, 1-4, 2-1, 2-3, 2-4, 3-1, 3-2, 4-1, 4-2\}$ , whereas the third column has all the pairs of devices that include device 2 and device 3, which is  $\{1-2, 1-3, 2-1, 2-3, 2-4, 3-1, 3-2, 3-4, 4-2, 4-3\}$ , and so on.

## VI. Experimental Results

This section outlines the simulation settings and the evaluation metrics used to assess the resource allocation performance across various network scenarios. We compare the performance of hybrid RF-OWC networks against RF networks under diverse conditions. Furthermore, we benchmark the proposed DGET framework against optimal solutions obtained via the optimization model in (P1) to demonstrate its effectiveness, scalability, and robustness towards partial system parameter knowledge.

### A. Simulation Setup and Evaluation Metrics

#### 1) System Parameters and Experimental Setup

The simulation parameters for RF, OWC, the proposed DGET, and the overall system are included in Table 2. All the simulations in this section are achieved using Monte-Carlo with 10,000 iterations. All algorithms are implemented in a Python 3.10 environment and run on a 72-socket Intel(R) Xeon(R) Gold 5220 CPU @ 2.20GHz with 256GB of RAM. For solving the MILP problem, we use the academic CPLEX, an off-the-shelf optimization software package.

We consider a time step of  $\tau = 50\text{ms}$  and a total simulation time of 10 time steps, hence  $|\mathcal{T}| = 500\text{ms}$ . The distance between the different IoT devices is randomly

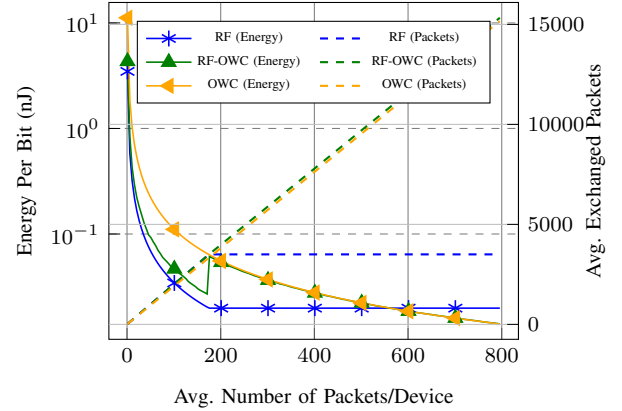


FIGURE 7. Energy per bit in logarithmic scale (marker) and avg. exchanged packets (dashed) vs. avg. number of packets per device for RF, OWC, and hybrid RF-OWC systems.

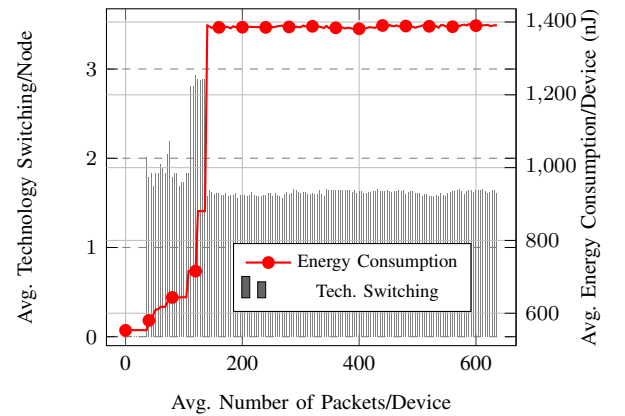


FIGURE 8. Avg. technology switching/energy consumption rate per device for hybrid RF-OWC.

generated from  $\mathcal{U}(3, 20)$  meters. The total available energy of all nodes also follows the uniform distribution  $\mathcal{U}(0.05, 0.1)$  joules for both RF and OWC technologies. The data arrival process from each device  $i$  is modeled as a Bernoulli process, as in [61]. Accordingly, we generate the communication matrix  $\mathbf{P}$  such that each entry  $\mathbf{P}_{a,b}$  represents a potential message transmission from device  $a$  to device  $b$  at a given time step. Each APs-to-node pair is independently sampled from a Bernoulli distribution with probability 0.7. Similarly, node-to-node communications are generated with a Bernoulli probability of 0.3. Each time slot includes multiple independent packet generation events per device, each following a Bernoulli process. Messages are constrained to have a maximum duration of 4 time steps, i.e.,  $(\phi_{i,j}^{f,l})_e - (\phi_{i,j}^{f,l})_s \leq 4$ .

We model link availability as a two-state Markov process to capture temporal correlation in outages. Each RF and OWC link alternates between an available state and a blocked state. For OWC links, the blocked state represents object-shadowing events with an average duration between 3 and 8 time steps, while for RF links, the blocked state represents congestion-induced interruptions with an average duration between 2 and 6 time steps. The number of available types of data is set to  $|\mathcal{L}| = 2$ . Relying on the same sensitivity

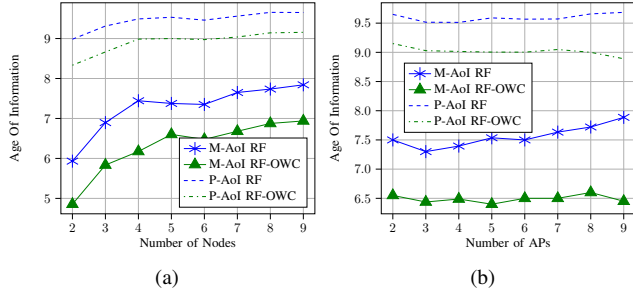


FIGURE 9. (a) M-AoI and P-AoI vs. number of IoT nodes when  $|\mathcal{N}_{AP}| = 3$  and (b) M-AoI and P-AoI vs. number of APs when  $|\mathcal{N}_d| = 5$ , for both hybrid RF-OWC and RF systems.

analysis approach from our previous work [1], we choose the value of  $\alpha_1 = 0.35$  and hence,  $\alpha_2 = 0.65$ .

## 2) Evaluation Metrics

We evaluate our system using a range of performance metrics that capture both network-level efficiency and model-level learning behavior.

First, we consider the linear AoI [62], the most widely used and recognized metric to measure the freshness of information. AoI is defined as the difference between the current time and the time at which the last successfully received update was generated at the source [62], [63]. At time  $k \in \mathcal{T}$ , if the freshest update received by device  $j \in \mathcal{N}$  from device  $i \in \mathcal{N}$  was generated at  $u(k) = \left(\phi_{i,j}^{f,l}\right)_s$ , then the AoI is defined as:

$$\Delta(k) = k - u(k). \quad (29)$$

AoI increases linearly with time and resets upon the reception of a newer update. To evaluate AoI performance, we consider two metrics: the Mean AoI (M-AoI) and the Peak AoI (P-AoI). Given a set of update reception times  $k_1, k_2, \dots, k_n$ , the M-AoI and P-AoI are defined as:

$$\text{M-AoI} = \frac{1}{|\mathcal{T}|} \int_0^{|\mathcal{T}|} \Delta(k) dk, \quad (30)$$

$$\text{P-AoI} = \frac{1}{|\mathcal{N}|} \sum_{i \in \mathcal{N}} \Delta(k_i^-). \quad (31)$$

M-AoI reflects the average age of information across the network, indicating the system's overall freshness. P-AoI captures the maximum age just before an update is received, offering insight into the worst-case data staleness.

Furthermore, we evaluate the network's reliability using energy-centric indicators, such as total energy consumption and energy per bit, and communication-centric indicators, such as the successful transmission rate and overall network exchanged packets. For all simulations with OWC technology, the communication-related energy is considered while excluding illumination energy, as reflected by the scaling factor  $\kappa = 0.3$ .

For evaluating the performance of the DGET model, we monitor the consistency loss, classification loss, and total model loss in training and validation. We also evaluate

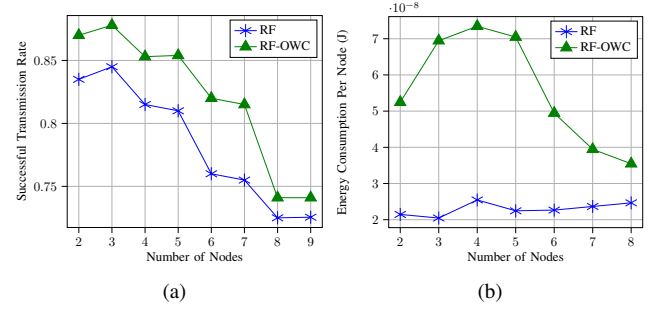


FIGURE 10. (a) Successful transmission rate and (b) energy consumption rate per device vs. number of IoT nodes for RF and RF-OWC with  $|\mathcal{N}_{AP}| = 2$ .

the GATs embeddings and the reconstructed GraphSAGE embeddings and present the classification accuracy and AoI of the resultant DGET resource allocation. Moreover, we assess the confusion matrix to showcase the reliability of class-wise predictions and perform a complexity analysis for running time to analyze the computational complexity of the different approaches. Finally, we investigate the DGET robustness towards channel imperfections.

## B. Hybrid RF-OWC Regime Analysis

We solve (P1) for a network setup of  $|\mathcal{N}_{AP}| = 2$  and  $|\mathcal{N}_d| = 3$  under three configurations: RF only, OWC only, and hybrid RF-OWC, and present a comparative analysis in terms of energy efficiency and avg. successful packet exchange, as shown in Fig. 7. At low traffic levels, RF achieves the best energy efficiency. However, as the number of packets per device increases, RF performance saturates. The RF-OWC system initially offers better energy efficiency than OWC and continues to perform reliably beyond the RF saturation point (around 180 packets). Although RF-OWC starts with higher energy consumption than RF, it improves steadily and surpasses RF at approximately 600 packets per device. Overall, RF-OWC demonstrates superior scalability and supports higher traffic volumes while maintaining energy-efficient communication.

To further understand the behavior of the hybrid system under varying traffic loads, Fig. 8 shows the relationship between the number of technology switches per device and the corresponding energy consumption as the average packet load increases for the same network size setup. At low traffic levels, RF is predominantly used due to its energy efficiency. As the load increases, the system frequently switches between RF and OWC to manage the growing demand. However, beyond approximately 170 packets per device, the number of switches stabilizes, indicating that the system consistently relies on the same technology for communication. This behavior aligns with the observation in Fig. 7, where OWC becomes more favorable under high traffic conditions. In all the subsequent simulations, a default network generation rate of 100 packets per device is adopted to ensure that both RF and OWC communication modes are actively utilized.

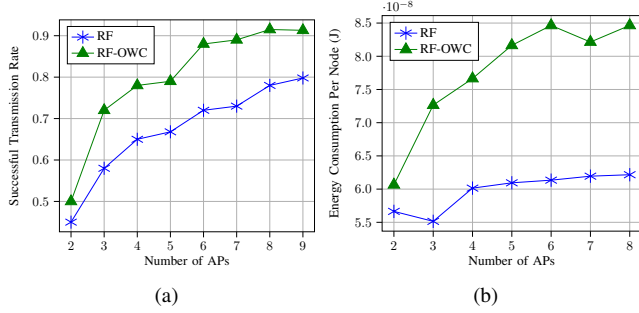


**FIGURE 11. (a) Successful transmission rate and (b) energy consumption rate per device vs. number of APs for RF and hybrid RF-OWC systems with  $|\mathcal{N}_d| = 5$ .**

### C. Optimization Results

In Fig. 9, we analyze the Peak Age of Information (P-AoI) and Mean Age of Information (M-AoI) metrics for both RF and RF-OWC systems. In Fig. 9-(a), we fix the number of APs to  $|\mathcal{N}_{AP}| = 3$  and vary the number of nodes. Both metrics increase as the number of nodes grows, indicating a decline in information timeliness with network scale. Notably, the RF-OWC system achieves approximately 14% lower AoI values compared to the RF-only system. In Fig. 9-(b), we fix the number of nodes to  $|\mathcal{N}_d| = 5$  and vary the number of APs. The M-AoI and P-AoI slightly increase in the RF system with the increase of APs but remain somehow stable in the RF-OWC system. This is attributed to the predominance of node-to-APs traffic and the ability of newly introduced APs in the RF-OWC system to leverage OWC, thereby alleviating RF congestion and preserving overall information freshness.

In Fig. 10, we compare the performance of RF and hybrid RF-OWC systems with the number of APs fixed at  $|\mathcal{N}_{AP}| = 2$ . Both systems show a general decrease in successful transmission rate as the number of nodes increases; however, the hybrid RF-OWC system consistently achieves higher success rates. The performance gap between the two systems narrows as the network size grows. Regarding energy consumption, the RF-OWC system initially experiences an increase followed by a decline, indicating that newly added nodes may no longer access the OWC channel, likely due to channel saturation by existing nodes and the limited number of APs. As a result, energy consumption in the RF-OWC system trends closer to that of the RF-only system. Meanwhile, the RF system's energy consumption remains relatively stable across different node counts.

Fig. 11 explores a scenario with a fixed number of  $|\mathcal{N}_d| = 5$  IoT nodes while varying the number of APs. The hybrid RF-OWC system again shows the highest successful transmission rate, which improves as the number of APs increases, reflecting more communication opportunities. Energy consumption rises for both RF-OWC and RF systems, with a notably sharper increase observed in the hybrid RF-OWC configuration. This sharper increase is attributed to the

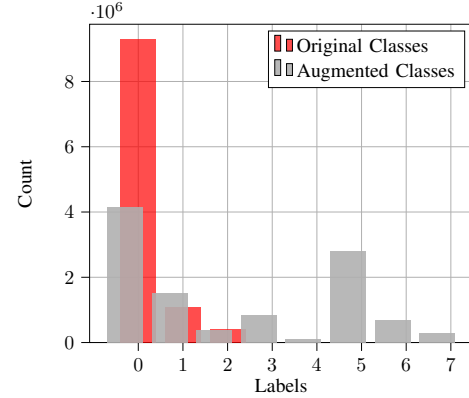


**FIGURE 12. Histogram of labels before and after label augmentation for a dataset of  $|\mathcal{N}_d| = 5$  and  $|\mathcal{N}_{AP}| = 2$ .**

added APs being OWC-enabled, leading to more frequent reliance on the OWC interface for communication.

### D. Training of DGET

In order to train the proposed DGET model, we generate approximately 500,000 solution instances by solving (P1) and recording the communication evolution over the time horizon  $\mathcal{T}$ . Each solution yields a sequence of  $|\mathcal{T}|$  known-labeled graph pairs. As shown in the histogram in Fig. 12, the dataset exhibits a significant class imbalance, predominantly in favor of class 0. This skew arises naturally from the data generation process and the system constraints, where most time steps involve no active communication. Such an imbalance can severely bias a machine learning model, degrading its performance in minority classes. To mitigate this, we augment the dataset by leveraging available communication links, thereby rebalancing the label distribution and expanding it to 8 classes (cf. Section V-E). The DGET training parameters are provided in Table 2. Notably, we apply the post-processing strategy during validation, as in testing, to ensure consistency and fair evaluation of generalization performance. We also employ the OneCycle learning rate scheduler. The learning rate starts at  $2 \times 10^{-4}$ , increases to a peak of  $5 \times 10^{-3}$ , and then decays to a final value of  $5 \times 10^{-7}$ . This schedule enables rapid initial exploration followed by granular convergence in the later training phases. Additionally, we introduce a time-varying consistency loss coefficient  $\lambda$  that decays linearly over the training epochs with  $\lambda = 0.5 \times \left(1 - \frac{\text{epoch}}{\text{epochs}}\right)$ . This shifts the model's focus to optimizing stable representations early on, then prioritizes classification performance in later epochs. The DGET model is trained on 8 NVIDIA GeForce RTX 2080 Ti GPUs, each with 11 GB of GDDR6 memory. For positional encoding, we adopt a learnable approach by initializing random vectors for each device's embeddings and allowing the model to optimize them during training. Temporal encoding is implemented using sinusoidal functions to capture periodic patterns, as described in [64].

Fig. 13-(a) shows the DGET's training and validation loss curves, along with the breakdown of individual components:

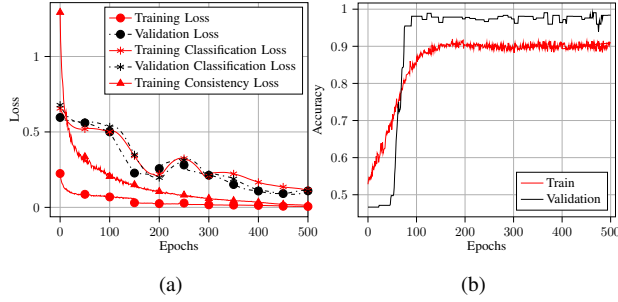


FIGURE 13. (a) Overall training and validation losses, training and validation losses for classification, and training loss for consistency vs. epochs, and (b) overall training and validation accuracy vs. epochs.

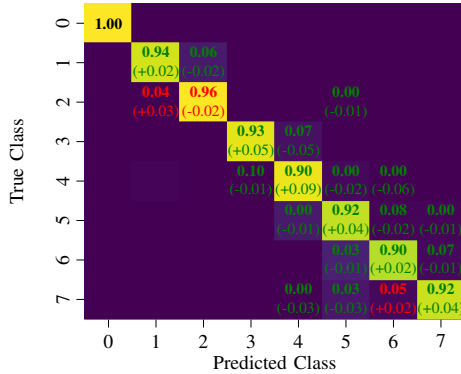


FIGURE 14. Classification confusion matrix on test data after post-processing highlighted by green color if the change is positive with post-processing or red otherwise.

the consistency and classification losses. The overall training loss exhibits a sharp decline during the initial training phase, primarily driven by the consistency loss, which carries greater weight early in training. This phase is followed by stabilization after approximately 250 epochs. The classification loss, though more variable throughout the training process, steadily decreases and stabilizes at a low value. The validation loss, in contrast, reflects only the classification component, as the consistency loss is not computed during validation (i.e., validation uses only known data and does not involve unlabeled or predicted graph embeddings). Such separation ensures that validation directly assesses the model’s classification ability without the influence of consistency regularization.

Fig. 13-(b) depicts the training and validation classification accuracy curves. Initially, the validation accuracy lags behind the training accuracy. This discrepancy arises not only from the model still learning but also from the inclusion of post-processing during validation. In the early epochs, the post-processing logic often fails to improve prediction accuracy because it relies on structural coherence (cf. Section V-E), which is not yet established in the model’s output. Consequently, post-processing can even slightly degrade accuracy in the initial stages. However, around epoch 70, validation accuracy with post-processing begins to surpass raw training accuracy. As training progresses and the model starts generating more consistent and meaningful predictions, the

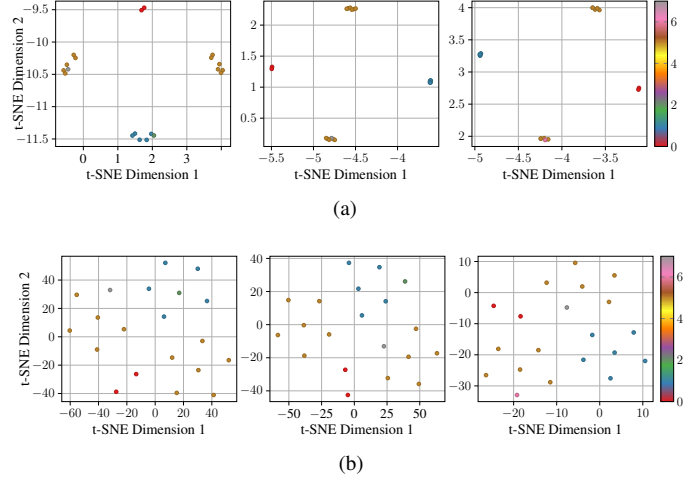


FIGURE 15. t-SNE visualization of transductive (top) and inductive (bottom) embeddings across three snapshots ( $|\mathcal{T}| = 3$ ), with each column representing one snapshot in time.

post-processing becomes increasingly effective, ultimately yielding nearly a 7% improvement in overall accuracy (while also accounting for the dropout effect).

Fig. 14 presents the confusion matrices for the DGET model before and after post-processing on hold-out 20% testing set. The green and red annotations in the matrix respectively highlight positive and negative changes, offering intuitive insights into where the model improved or regressed. The post-processing significantly improved classification performance, especially in reducing inter-class confusion for adjacent and similar classes. The diagonal elements, representing correct classifications, improved across nearly all classes, especially for Class 3 (0.87 to 0.96), Class 4 (0.52 to 0.97), and Class 7 (0.77 to 0.92). Off-diagonal confusions were also significantly reduced, such as class 3, which was misclassified as Class 4 in 7% of cases without post-processing.

To better illustrate the advantages of incorporating inductive learning on top of transductive embeddings, we visualize the learned representations using t-distributed Stochastic Neighbor Embedding (t-SNE) [65] projected into 2D space. This visualization offers a tangible view of how well the model captures class separability over time. As shown in the top row of Fig. 15, transductive embeddings exhibit low-variance features and tend to cluster tightly, making it harder to define a decision boundary distinguishing between communication classes. In contrast, the inductive embeddings in the bottom row are more dispersed, revealing a clearer and more structured separation between ground truth classes (e.g., no communication, RF, or OWC). This increased spread indicates a more generalizable feature space.

### E. Inference with DGET

In Table 3, we evaluate the performance of three communication configurations using  $|\mathcal{N}_d| = 9$  devices and  $|\mathcal{N}_{AP}| = 2$

**TABLE 3.** M-AoI and P-AoI for both RF (MILP), RF-OWC (MILP), and RF-OWC (DGET) configurations computed for the overall system, data type 1, and data type 2.

	RF (MILP)	RF-OWC (MILP)	RF-OWC (DGET)
All Data	M-AoI: 7.3 P-AoI: 8.9	M-AoI: 6.1 P-AoI: 7.8	M-AoI: 6.4 P-AoI: 8
Data Type 1	M-AoI: 7.5 P-AoI: 8.9	M-AoI: 6 P-AoI: 7.7	M-AoI: 6.2 P-AoI: 7.9
Data Type 2	M-AoI: 6.9 P-AoI: 8.9	M-AoI: 6.3 P-AoI: 8.1	M-AoI: 6.6 P-AoI: 8.3

access points, following the training and simulation setup previously described. The results compare M-AoI and P-AoI across: (1) an RF-only system optimized via MILP, (2) a hybrid RF-OWC system also optimized via MILP, and (3) a hybrid RF-OWC system where scheduling is handled by the DGET model.

The optimized RF-OWC configuration yields the best performance, with a M-AoI of 6.1 and a P-AoI of 7.8, showing clear improvements over the RF-only baseline (M-AoI of 7.3, P-AoI of 8.9). These gains are consistent across both data categories (i.e., Data Type 1 and Data Type 2). The DGET model exhibits slightly higher AoI values (e.g., M-AoI of 6.4 vs. 6.1 for all data), but the differences are minor. This indicates that despite not being globally optimal, the learned DGET policy can closely approximate the performance of the optimization-based solution in terms of AoI.

In Fig.16, we evaluate the running time to highlight the inference computational efficiency of the DGET compared to the optimization solver. We maintain the ratio of 1 APs per 3 IoT nodes, and increase the overall number of IoT devices, respectively. The RF-OWC system, which incorporates both RF and optical wireless communication capabilities, shows the highest computational cost due to the added complexity of managing multi-band interfaces and link selection processes. In contrast, the traditional RF system presents a more moderate increase in execution time, reflecting its simpler communication model. The DGET framework consistently outperforms both baseline methods in terms of execution efficiency. Despite incorporating advanced graph-based reasoning and sequence modeling, it maintains the lowest running time across all network sizes, demonstrating a polynomial trend that is estimated  $O(|\mathcal{N}|^2 \varphi)$  with  $\varphi$  is the aggregated hidden dimensionality across model components.

In Fig.17, we evaluate DGET's robustness against missing or outdated link information for RF-OWC network. We replace edge weights in the input graph  $\mathcal{G}_k^l(\mathcal{V}, \mathcal{E})$  with deprecated values from previous snapshots to simulate outdated channel information of the allowed communication technology. The snapshots used for replacement are non-subsequent snapshots, i.e., not directly adjacent in time, preventing the carryover of stale information across consecutive updates. We evaluate three scenarios in which edge weight replace-

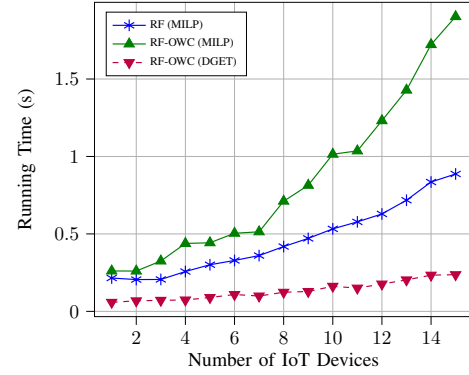


**FIGURE 16.** Running time (s) of the RF, RF-OWC, and DGET model vs. number of IoT Devices in the network.

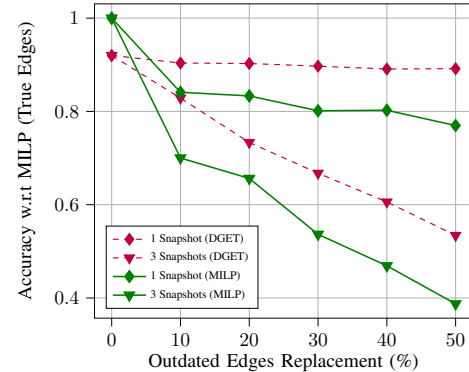


**FIGURE 17.** Impact of edge staleness on DGET prediction (link class) accuracy when using outdated allowed technologies for RF-OWC network with  $|\mathcal{T}| = 10$ .

ment occurs in 1, 2, or 3 randomly selected non-subsequent snapshots among  $|\mathcal{T}| = 10$ , with the overall replacement rate uniformly varied between 10% and 50%. Across all settings, DGET consistently outperforms the MILP baseline. For example, when 20% of all edges are outdated across 2 snapshots, DGET maintains nearly 90% accuracy, whereas MILP experiences a significantly sharper decline in performance. This behavior highlights a fundamental limitation of the optimization-based approach. Although the MILP is solved optimally with respect to the provided input parameters, it implicitly assumes perfectly accurate channel state information. As a result, when the optimization is supplied with stale channel realizations, it effectively solves an optimal solution to a mismatched problem, without accounting for the stochastic temporal evolution of links or the uncertainty in their availability across snapshots. In contrast, DGET leverages historical information and learned temporal patterns to adapt its decisions under uncertainty, enabling more robust link allocation in the presence of outdated or imperfect channel knowledge.

## VII. Conclusion and Future Work

This paper investigated the resource allocation in hybrid RF-OWC IoT networks through deterministic optimization and a designed DGET framework that combines GNNs with Transformer-based learning to address the computational

challenges of traditional MILP optimization. Experimental results showed that hybrid RF-OWC achieves significant improvements in AoI while maintaining comparable energy efficiency to the RF system, making it highly effective in environments where timely data delivery is critical. Moreover, DGET achieves near-optimal scheduling with notably reduced computational overhead and robustness to outdated channel information. While DGET is demonstrated in the context of RF and optical communication, the proposed framework can, in principle, be applied to any dual-band communication system, a direction that also aligns with current research trends in 6G networks, with dual-band and multi-band operation being increasingly explored. Future research will focus on extending DGET to mobile and outdoor environments, integrating real-time feedback mechanisms, and validating the approach on hardware testbeds and physical IoT infrastructures. Additionally, incorporating energy-harvesting-aware scheduling policies will be a key direction to support sustainable and self-powered IoT operations in resource-constrained networks.

## REFERENCES

- [1] A. Hamrouni, S. Pollin, and H. Sallouha, "AoI in Context-Aware hybrid Radio-Optical IoT networks," in *2024 IEEE Global Communications Conference: IoT and Sensor Networks (Globecom 2024 IoTNS)*, Cape Town, South Africa, Dec. 2024, p. 5.98.
- [2] P. Rajasekar, R. S. Bhosale, I. C. S. K. V. P. Kumari N, and R. M., "Real-time stream processing in iot environments," in *2024 Ninth International Conference on Science Technology Engineering and Mathematics (ICONSTEM)*, 2024, pp. 1–5.
- [3] G. Rathee, C. A. Kerrache, C. T. Calafate, M. Bilal, and H. Song, "Smart: A secure remote sensing solution for smart cities' urban areas," *IEEE Sensors Journal*, vol. 24, no. 7, pp. 11 553–11 561, 2024.
- [4] Z. Ling, F. Hu, H. Zhang, and Z. Han, "Age-of-information minimization in healthcare iot using distributionally robust optimization," *IEEE Internet of Things Journal*, vol. 9, no. 17, pp. 16 154–16 167, 2022.
- [5] J. Tang, F. Chen, J. Li, and Z. Liu, "Learn to schedule: Data freshness-oriented intelligent scheduling in industrial iot," *IEEE Transactions on Cognitive Communications and Networking*, pp. 1–1, 2024.
- [6] D. Van Leemput, A. Sabovic, K. Hammoud, J. Famaey, S. Pollin, and E. De Poorter, "Energy harvesting for wireless iot use cases: A generic feasibility model and tradeoff study," *IEEE Internet of Things Journal*, vol. 10, no. 17, pp. 15 025–15 043, 2023.
- [7] R. Verma, S. Gautam, N. Singh Bal, S. Kumar, and N. Saeed, "Iot-enabled energy-efficient and long-range solution for remote patient monitoring using bluetooth low energy 5.x," *IEEE Journal of Radio Frequency Identification*, vol. 9, pp. 527–541, 2025.
- [8] C. Hwang and J. Fan, "Modeling and mitigation of radio frequency interference for wireless devices," *IEEE Electromagnetic Compatibility Magazine*, vol. 12, no. 1, pp. 87–92, 2023.
- [9] A. F. Harris III, V. Khanna, G. Tuncay, R. Want, and R. Kravets, "Bluetooth low energy in dense iot environments," *IEEE Communications Magazine*, vol. 54, no. 12, pp. 30–36, 2016.
- [10] M. A. Saeidi, H. Tabassum, and M.-S. Alouini, "Multi-band wireless networks: Architectures, challenges, and comparative analysis," *IEEE Communications Magazine*, vol. 62, no. 1, pp. 80–86, 2024.
- [11] M. Utsch, B. Böckling, W. Kiess, T. Bauschert, A. Baumgartner, and S. Baumgartner, "High-availability in iot applications through dual connectivity: Integrating lorawan and nb-iot," in *2024 20th International Conference on the Design of Reliable Communication Networks (DRCN)*, 2024, pp. 151–158.
- [12] Y. C. Lee, H. Ramiah, A. Choo, K. K. P. Churchill, N. S. Lai, C. C. Lim, Y. Chen, P.-I. Mak, and R. P. Martins, "High-performance multi-band ambient rf energy harvesting front-end system for sustainable iot applications—a review," *IEEE Access*, vol. 11, pp. 11 143–11 164, 2023.
- [13] M. Katz, T. Paso, K. Mikhaylov, L. Pessoa, H. Fontes, L. Hakola, J. Leppänen, E. Carlos, G. Dolmans, J. Rufo, M. Drzewiecki, H. Sallouha, B. Napier, A. Branquinho, and K. Eder, "Towards truly sustainable iot systems: the superiot project," *Journal of Physics: Photonics*, vol. 6, no. 1, p. 011001, jan 2024. [Online]. Available: <https://doi.org/10.1088/2515-7647/ad1c6a>
- [14] M. Z. Chowdhury, M. K. Hasan, M. Shahjalal, M. T. Hossan, and Y. M. Jang, "Optical wireless hybrid networks: Trends, opportunities, challenges, and research directions," *IEEE Communications Surveys & Tutorials*, vol. 22, no. 2, pp. 930–966, 2020.
- [15] A. F. Raouf, C. K. Anjinappa, and G. I., "Optimal design of energy-harvesting hybrid vlc/rf networks," in *2022 IEEE Globecom Workshops (GC Wkshps)*, 2022, pp. 705–710.
- [16] L. Rodrigues, M. Figueiredo, L. N. Alves, and Z. Ghassemlooy, "Visible light communication systems architectures for the internet of things," in *2023 IEEE 9th World Forum on Internet of Things (WF-IoT)*, 2023, pp. 1–2.
- [17] IoT Analytics. (2024, September) Number of connected iot devices growing 13% to 18.8 billion globally. Accessed: 2025-06-05. [Online]. Available: <https://iot-analytics.com/number-connected-iot-devices/>
- [18] N. Guler, "Vertical handover-based hybrid radio frequency/visible light communication scheme for e-health applications (who-hea)," *Engineered Science*, vol. 33, p. 1252, 2025. [Online]. Available: <http://dx.doi.org/10.30919/es1252>
- [19] A. Zakeri, M. Moltafet, M. Leinonen, and M. Codreanu, "Minimizing the aoI in resource-constrained multi-source relaying systems: Dynamic and learning-based scheduling," *IEEE Transactions on Wireless Communications*, vol. 23, no. 1, pp. 450–466, 2024.
- [20] M. Katz, T. Paso, K. Mikhaylov, L. Pessoa, H. Fontes, L. Hakola, J. Leppänen, E. Carlos, G. Dolmans, J. Rufo, M. Drzewiecki, H. Sallouha, B. Napier, A. Branquinho, and K. Eder, "Towards truly sustainable iot systems: the superiot project," *Journal of Physics: Photonics*, vol. 6, no. 1, p. 011001, 2024.
- [21] C. Luo, J. Ji, Q. Wang, X. Chen, and P. Li, "Channel state information prediction for 5g wireless communications: A deep learning approach," *IEEE Transactions on Network Science and Engineering*, vol. 7, no. 1, pp. 227–236, 2020.
- [22] G. Liu, Y. Xu, Z. He, Y. Rao, J. Xia, and L. Fan, "Deep learning-based channel prediction for edge computing networks toward intelligent connected vehicles," *IEEE Access*, vol. 7, pp. 114 487–114 495, 2019.
- [23] W. Jiang and H. D. Schotten, "Deep learning for fading channel prediction," *IEEE Open Journal of the Communications Society*, vol. 1, pp. 320–332, 2020.
- [24] Q. Zhou, W. Jiang, D. Wang, and H. D. Schotten, "Deep learning-based signal-to-noise ratio prediction for realistic wireless communication," in *2022 IEEE 95th Vehicular Technology Conference: (VTC2022-Spring)*, 2022, pp. 1–5.
- [25] A. Del Pia, S. Dey, and M. Molinaro, "Mixed-integer quadratic programming is in np," *Mathematical Programming*, vol. 162, 07 2014.
- [26] Y. Shen, J. Zhang, S. H. Song, and K. B. Letaief, "Graph neural networks for wireless communications: From theory to practice," *IEEE Transactions on Wireless Communications*, vol. 22, no. 5, pp. 3554–3569, 2023.
- [27] A. Vaswani, N. Shazeer, N. Parmar, J. Uszkoreit, L. Jones, A. N. Gomez, L. Kaiser, and I. Polosukhin, "Attention is all you need," 2023. [Online]. Available: <https://arxiv.org/abs/1706.03762>
- [28] L. Anghinoni, Y.-t. Zhu, D. Ji, and L. Zhao, "Transgnn: A transductive graph neural network with graph dynamic embedding," in *2023 International Joint Conference on Neural Networks (IJCNN)*, 2023, pp. 1–8.
- [29] H. Tang and Y. Liu, "Towards understanding the generalization of graph neural networks," 2023. [Online]. Available: <https://arxiv.org/abs/2305.08048>
- [30] W.-D. Li, K. Hu, C. Larsen, Y. Wu, S. Alford, C. Woo, S. M. Dunn, H. Tang, M. Naim, D. Nguyen, W.-L. Zheng, Z. Tavares, Y. Pu, and K. Ellis, "Combining induction and transduction for abstract reasoning," 2024. [Online]. Available: <https://arxiv.org/abs/2411.02272>
- [31] T. Tang, L. Shi, Q. Li, and Z. Xiong, "Sustainability-driven resource allocation for slipt-assisted hybrid vlc/rf iot systems," *IEEE Wireless Communications Letters*, vol. 13, no. 6, pp. 1765–1769, 2024.
- [32] M. Fakirah, S. Leng, M. Mohammad, A. Abualnor, and M. L. Betalo, "Improving user data rate performance for hybrid rf/vlc outdoor vehicular communications," in *2022 IEEE 22nd International Conference on Communication Technology (ICCT)*, 2022, pp. 812–816.

- [33] M. Obeed *et al.*, “Joint optimization of power allocation and load balancing for hybrid vlc/rf networks,” *Journal of Optical Communications and Networking*, vol. 10, no. 5, pp. 553–562, 2018.
- [34] Y. Xiao, P. D. Diamantoulakis, Z. Fang, L. Hao, Z. Ma, and G. K. Karagiannidis, “Cooperative hybrid vlc/rf systems with slipt,” *IEEE Transactions on Communications*, vol. 69, no. 4, pp. 2532–2545, 2021.
- [35] Y. Guo, K. Xiong, Y. Lu, D. Wang, P. Fan, and K. B. Letaief, “Achievable information rate in hybrid vlc-rf networks with lighting energy harvesting,” *IEEE Transactions on Communications*, vol. 69, no. 10, pp. 6852–6864, 2021.
- [36] A. M. Alenezi and K. A. Hamdi, “Reinforcement learning approach for hybrid wifi-vlc networks,” in *2020 IEEE 91st Vehicular Technology Conference (VTC2020-Spring)*, 2020, pp. 1–5.
- [37] M. Khalili, M. Katz, H. Sallouha, S. Pollin, and K. Mikhaylov, “Multi-attribute handover in optical wireless and radio frequency heterogeneous networks: A decentralized approach,” in *2025 IEEE Wireless Communications and Networking Conference (WCNC)*, 2025, pp. 1–6.
- [38] A. Hamrouni, H. Ghazzai, T. Alelyani, and Y. Massoud, “Low-complexity recruitment for collaborative mobile crowdsourcing using graph neural networks,” *IEEE Internet of Things Journal*, vol. 9, no. 1, pp. 813–829, 2022.
- [39] A. Hamrouni, A. Khanfor, H. Ghazzai, and Y. Massoud, “Context-aware service discovery: Graph techniques for iot network learning and socially connected objects,” *IEEE Access*, vol. 10, pp. 107330–107345, 2022.
- [40] A. Hamrouni, H. Ghazzai, and Y. Massoud, “Service discovery in social internet of things using graph neural networks,” in *2022 IEEE 65th International Midwest Symposium on Circuits and Systems (MWSCAS)*, 2022, pp. 1–4.
- [41] Y. Yang, Z. Zhang, Y. Tian, R. Jin, and C. Huang, “Implementing graph neural networks over wireless networks via over-the-air computing: A joint communication and computation framework,” *IEEE Wireless Communications*, vol. 30, no. 3, pp. 62–69, 2023.
- [42] V. Kansal, L. Hussein, A. Vargas-Chavarrea, N. Varshney, G. Sharma, and A. K. Rao, “Real-time environmental monitoring and prediction in iot networks with graph neural networks,” in *2024 International Conference on Communication, Computer Sciences and Engineering (IC3SE)*, 2024, pp. 1628–1633.
- [43] J. Suárez-Varela, P. Almasan, M. Ferriol-Galmés, K. Rusek, F. Geyer, X. Cheng, X. Shi, S. Xiao, F. Scarselli, A. Cabellos-Aparicio, and P. Barlet-Ros, “Graph neural networks for communication networks: Context, use cases and opportunities,” *IEEE Network*, vol. 37, no. 3, pp. 146–153, 2023.
- [44] P. Cheng, G. Chen, and Z. Han, “Graph neural networks based resource allocation in heterogeneous wireless networks,” in *Proceedings of the 7th International Conference on Intelligent Information Processing*, ser. ICIIP '22. New York, NY, USA: Association for Computing Machinery, 2023. [Online]. Available: <https://doi.org/10.1145/3570236.3570293>
- [45] M. Eisen and A. Ribeiro, “Optimal wireless resource allocation with random edge graph neural networks,” *IEEE Transactions on Signal Processing*, vol. 68, p. 2977–2991, 2020. [Online]. Available: <http://dx.doi.org/10.1109/TSP.2020.2988255>
- [46] T. Chen, X. Zhang, M. You, G. Zheng, and S. Lambotaran, “A gnn-based supervised learning framework for resource allocation in wireless iot networks,” *IEEE Internet of Things Journal*, vol. 9, no. 3, pp. 1712–1724, 2022.
- [47] Z. Zhao, G. Verma, C. Rao, A. Swami, and S. Segarra, “Distributed scheduling using graph neural networks,” in *ICASSP 2021 - 2021 IEEE International Conference on Acoustics, Speech and Signal Processing (ICASSP)*, 2021, pp. 4720–4724.
- [48] A. Goldsmith, *Wireless Communications*. Cambridge University Press, 2005.
- [49] K. Hammoud, D. Schreurs, S. Pollin, and Z. Cui, “A joint opportunistic energy harvesting and communication system using vlc for battery-less pv-equipped iot,” in *2023 IEEE International Conference on Communications Workshops (ICC Workshops)*, 2023, pp. 1926–1931.
- [50] H. Lu, Z. Su, and B. Yuan, “Snr and optical power distribution in an indoor visible light communication system,” in *2014 7th International Congress on Image and Signal Processing*, 2014, pp. 1063–1067.
- [51] D. A. B. Miller, “Energy consumption in optical modulators for interconnects,” *Opt. Express*, vol. 20, no. S2, pp. A293–A308, Mar 2012. [Online]. Available: <https://opg.optica.org/oe/abstract.cfm?URI=oe-20-102-A293>
- [52] G. P. McCormick, “Computability of global solutions to factorable nonconvex programs: Part i — convex underestimating problems,” *Mathematical Programming*, vol. 10, no. 1, pp. 147–175, Dec. 1976. [Online]. Available: <https://doi.org/10.1007/BF01580665>
- [53] M. Cococcioni and L. Fiaschi, “The big-m method with the numerical infinite m,” *Optimization Letters*, vol. 15, 10 2021.
- [54] D. R. Morrison, S. H. Jacobson, J. J. Sauppe, and E. C. Sewell, “Branch-and-bound algorithms: A survey of recent advances in searching, branching, and pruning,” *Discrete Optimization*, vol. 19, pp. 79–102, 2016. [Online]. Available: <https://www.sciencedirect.com/science/article/pii/S1572528616000062>
- [55] G. Ciano, A. Rossi, M. Bianchini, and F. Scarselli, “On inductive–transductive learning with graph neural networks,” *IEEE Transactions on Pattern Analysis and Machine Intelligence*, vol. 44, no. 2, pp. 758–769, 2022.
- [56] N. Mu, D. Zha, Y. He, and Z. Tang, “Graph attention networks for neural social recommendation,” in *2019 IEEE 31st International Conference on Tools with Artificial Intelligence (ICTAI)*, 2019, pp. 1320–1327.
- [57] W. L. Hamilton, R. Ying, and J. Leskovec, “Inductive representation learning on large graphs,” 2018. [Online]. Available: <https://arxiv.org/abs/1706.02216>
- [58] P. Veličković, G. Cucurull, A. Casanova, A. Romero, P. Liò, and Y. Bengio, “Graph attention networks,” 2018. [Online]. Available: <https://arxiv.org/abs/1710.10903>
- [59] Y. Chen, J. Huang, H. Xu, J. Guo, and L. Su, “Road traffic flow prediction based on dynamic spatiotemporal graph attention network,” *Scientific Reports*, vol. 13, no. 1, p. 14729, 2023. [Online]. Available: <https://doi.org/10.1038/s41598-023-41932-6>
- [60] J. Kim, J. Jang, H. Park, and S. Jeong, “Structured consistency loss for semi-supervised semantic segmentation,” 2021. [Online]. Available: <https://arxiv.org/abs/2001.04647>
- [61] G. Li, G. Li, and Y. He, “Resolvable group target tracking via multi-bernoulli filter and its application to sensor control scenario,” *IEEE Transactions on Signal Processing*, vol. 70, pp. 6286–6299, 2022.
- [62] D. e. a. Deng, “Information freshness in a dual monitoring system,” in *2022 IEEE Global Communications Conference*, 2022, pp. 4977–4982.
- [63] Y. Chen, J. Wang, X. Wang, and J. Song, “Age of information optimization in multi-channel network with sided information,” *IEEE Communications Letters*, vol. 27, no. 3, pp. 1030–1034, 2023.
- [64] A. Bansal, K. Balaji, and Z. Lalani, “Temporal encoding strategies for energy time series prediction,” 2025. [Online]. Available: <https://arxiv.org/abs/2503.15456>
- [65] N. Rogovschi, J. Kitazono, N. Grozavu, T. Omori, and S. Ozawa, “t-distributed stochastic neighbor embedding spectral clustering,” in *2017 International Joint Conference on Neural Networks (IJCNN)*, 2017, pp. 1628–1632.